UNIVERSITY OF MANCHESTER

A NORTHERN SKY SURVEY AT 15GHZ

A dissertation submitted to The University of Manchester
for the degree of Master of Science by Research
in the Faculty of Science & Engineering
2021
Department of Physics and Astronomy

LAUREN DRAPER

Contents

Word count: 19,075

Abbreviations and Acronyms

9C	Ninth Cambridge Catalogue of Radio Sources
10C	Tenth Cambridge Catalogue of Radio Sources
AGN	Active Galactic Nuclei
AIPS	Astronomical Image Processing System
ALMA	Atacama Large Millimeter/submillimeter Array
AU	Astronomical unit
CBI	Cosmic Background Imager
CMB	Cosmic Microwave Background
dB	Decibel
DFT	Discrete Fourier transform
DM	Dispersion Measure
EOR	Epoch of Reionization
EVN	European VLBI Network
FT	Fourier Transform
FFT	Fast Fourier Transform
FWHM	Full Width at Half-Maximum
GBT	Green Bank Telescope
GPS	Global Positioning System
IAU	International Astronomical Union

IF	Intermediate Frequency
Jy	Jansky
LBA	Long-Baseline Array
LO	Local Oscillator
LOFAR	LOw Frequency ARray
LSMF	Least-Mean-Square Fit
LSR	Local Standard of Rest
LWA	Long Wavelength Array
MEM	Maximum Entropy Method
MERLIN	Multi-Element Radio Linked Interferometer Network
MERRA	Modern-Era Retrospective Analysis for Research and Applications (NASA program)
MMA	Millimeter Array (precursor to ALMA)
MSTID	MidScale Traveling Ionospheric Disturbance
NASA	National Aeronautics and Space Administration
NRAO	National Radio Astronomical Observatory (USA)
NVSS	NRAO VLA Sky Survey
OVLBI	Orbiting VLBI
RA	Right Ascension
RAM	Random Access Memory
RF	Radio Frequency

RFI	Radio Frequency Interference
RMS	Root Mean Square
SEFD	System Equivalent Flux Density
SI	System International
SKA	Square Kilometre Array
SMA	SubMillimeter Array
SNR	Signal-to-Noise Ratio
VLA	Very Large Array
VLBA	Very Long Baseline Array
VLBI	Very-Long-Baseline Interferometry
VSA	Very Small Array

Abstract

Due to the challenging nature of high frequency radio surveys, few have been performed, resulting in a poor knowledge of the high frequency radio source population. The Arcminute MicroKelvin Imager Small Array (AMI-SA) is now conducting a legacy survey of the complete Northern hemisphere at 15 GHz. This is the highest frequency survey conducted to date of the whole Northern hemisphere to a source detection level of 10 mJy. This project involved understanding of the calibration and imaging process of the AMI-SA drift scan data which were used to combine the different scans into a continuous map. The continuous maps were stitched together to generated larger maps of the Northern hemisphere and these maps were searched for sources and when the survey is completed a catalogue will be compiled. Modifications of the data pipeline were investigated with the aim to improved image quality through implementing self-calibration techniques to remove artefacts round bright sources. It was discovered that self-calibration significantly improved the image quality over what could be achieved with interleaved observations of a bright calibrator source, and the data reduction pipeline will be changed to include such a self-calibration step as standard. In future, identified sources will be followed up by observations with the AMI-LA to match NVSS resolution. A comparison of these results with NVSS will allow calculation of the radio spectral index distribution between 1.4 and 15 GHz and identification of any currently undiscovered inverted spectrum sources.

Declaration

No portion of the work referred to in the thesis has been submitted in support of an application for another degree or qualification of this or any other university or other institute of learning.

Copyright

i. The author of this thesis (including any appendices and/or schedules to this thesis) owns certain copyright or related rights in it (the Copyright) and she has given The University of Manchester certain rights to use such Copyright, including for administrative purposes.

ii. Copies of this thesis, either in full or in extracts and whether in hard or electronic copy, may be made only in accordance with the Copyright, Designs and Patents Act 1988 (as amended) and regulations issued under it or, where appropriate, in accordance with licensing agreements which the University has from time to time. This page must form part of any such copies made.

iii. The ownership of certain Copyright, patents, designs, trademarks and other intellectual property (the Intellectual Property) and any reproductions of copyright works in the thesis, for example graphs and tables (Reproductions), which may be described in this thesis, may not be owned by the author and may be owned by third parties. Such Intellectual Property and Reproductions cannot and must not be made available for use without the prior written permission of the owner(s) of the relevant Intellectual Property and/or Reproductions.

iv. Further information on the conditions under which disclosure, publication and commercialisation of this thesis, the Copyright and any Intellectual Property and/or Reproductions described in it may take place is available in the University IP Policy (see http://documents.manchester.ac.uk/DocumInfo.aspx?DocID=24420), in any relevant Thesis restriction declarations deposited in the University Library, The University Library’s regulations (see http://www.library.manchester.ac.uk/about/regulations/) and in the University’s policy on presentation of Theses

1. Introduction

1.1 The History of Radio Astronomy

Radio astronomy research began with the detection of radio emissions from the Milky Way by Jansky in 1931 (Thompson, Moran & Swenson, 1986). The first ever radio map of the sky was produced in 1942 by Reber in his back yard who had been intrigued by Karl Janksy’s observations of the Milky Way in 1932 (Pearson & Readhead, 1984). Reber was the world's only radio astronomer at the time, and his construction of the telescope and the sky surveys he did with it helped found the field of radio astronomy, revealing radio sources such as Cassiopeia A for the first time (Jackson, 2015).

The field evolved rapidly after World War II (Graham et al., 2021) with discoveries of objects such as pulsars, quasars, and radio galaxies (McKean, 2015). In more recent years, radio astronomical discoveries include the discovery of gravitational waves (Hulse & Taylor, 1993) and the discovery of the Cosmic Microwave Background CMB (Penzias & Wilson, 1978; Mather and Smoot, 2006). As radio observations expanded and more objects were discovered through radio emission, angular resolution increased from degrees to smaller than milli-arcseconds and receiver sensitivities advanced. The development of technology continues to contribute to the growth of radio astronomy which serves to provide a better understanding of the components and interactions of the universe and even the potential discovery of yet more unknown spatial objects (Briggs et al., 1999).

Radio astronomy operates at wavelengths at the longest end of the electromagnetic spectrum. Longer wavelengths lead to lower angular resolution θ as shown by the equation for angular resolution is λ/D where D is the size of the aperture (Jenkins & White, 2001).

Throughout the early period of the development of radio astronomy, radio telescopes' angular resolutions were around scales of arc-minutes at best, compared with the arc-second resolutions achievable by optical telescope. The development of interferometric techniques following methods first used by Michelson when applied to radio astronomy led to a massive shift in the way that radio astronomy was conducted (Louise M. Ker, 2010). These methods were further developed, resulting in Aperture Synthesis, mainly by M. Ryle and associates at Cambridge University (Kellermann and Moran, 2001). Aperture synthesis has allowed imaging with angular resolutions finer than milli-arcseconds with facilities such as the VLBA (Rottgering et al., 1994)

1.2 Single Dishes vs Interferometers

Current radio astronomy focuses primarily on single dish observation and interferometric observation. Early radio astronomical observations were conducted solely by single dishes, such as those of Jansky and Rebers and this technique is still used today in telescope such as the Five-hundred-meter Aperture Spherical Telescope (FAST) in China (Asaki et al., 2014), or the Arecibo radio telescope in Arecibo, Puerto Rico. Larger telescopes increase their angular resolutions proportional to their diameter with the cost of the telescope rising with approximately the cube of the dish diameter (Freeman, 1987) making single dish astronomy very expensive. The FAST telescope is the largest dish ever built, with a 500-meter diameter and cannot be moved, though its surface can be deformed to give a limited tracking capability on the sky (Fried, 1966)

Fortunately, radio astronomers have been able to utilise the techniques of interferometry to combine the two signals arriving at two antennas in order to study the resulting interference pattern and produce much higher angular resolutions through a process (Jaynes, 1957) known as aperture synthesis. The technique of aperture synthesis works by correlating the signal waves from the different telescopes on the principle that waves that coincide with the same phase will add to each other while two waves with opposite phase will cancel each other out. The result from interferometry is that the distance between two antennas, known as the telescope baseline, determines the angular resolution rather the diameter of the antennas themselves. An array of several antennas creates a combined telescope that is equivalent in resolution to a single antenna whose diameter equals the maximum spacing between the antennas.

1.3 What is a Radio Survey? / Why Conduct a Radio Survey?

Radio surveys are important astrophysical tool to provide large samples of galaxies for studying cosmology or galaxy evolution. Next generation radio surveys have the ability to transform radio astronomy with the discovery and study of tens of millions of previously unknown radio sources (Narayan et al., 1986). Sky surveys allow astronomers to catalogue celestial objects and perform statistical analyses on them without making prohibitively lengthy observations. Particular objects of interest can be found using previous survey images from radio surveys resulting in data obtained that is sufficient enough to make applying for additional telescope time entirely unnecessary cutting time and costs. (Condon et al., 1998).

In other cases, survey images help astronomers obtain observation time on larger, more powerful telescopes they otherwise might not have access to. The wide scope of surveys makes them ideal for searching for moving foreground objects such as asteroids and comets (Scaife et al. 2010). Additionally, existing survey images can be used to compare current observations to locate targets of interest; these could be targets which are in motion or of particular interest to the observer. Similarly, images of the same object taken by different surveys can be compared to detect transient events such as variable stars (Schwab, F. R., 1984).

1.4 Examples of Large Area Radio Surveys

1.4.1 NVSS

The NRAO VLA Sky Survey (NVSS) is a large area radio survey conducted at 1.4GHz between 1993 and 1996 to compile a list of sources covering the entire sky north of a 40 degree declination. The NVSS is based on 217,446 separately imaged snapshot observations of partially overlapping primary-beam areas. A catalogue of over 1.8 million sources has been produced which includes radio galaxies and quasars (Condon et al., 1998).

The catalogue is useful for a wide variety of different scientific projects including this project where it is expected that any identified sources over the course of this project will be followed up and imaged with the AMI Large Array to give angular resolution comparable to the NVSS survey. Comparing the AMI catalogue with NVSS will allow calculation of the radio spectral index distribution between 1.4 and 15 GHz and identification of any currently undiscovered inverted spectrum sources (Moshir et al 1992).

1.4.2 FIRST

The "Faint Images of the Radio Sky at Twenty-Centimeters" (FIRST) is a complementary survey to NVSS, also conducted by the VLA at 1.4 GHz. It surveyed a smaller area between 1993 and 2004 with higher resolution and greater sensitivity to yield a catalogue of about 800,000 sources. It found many sources that are not present in the NVSS catalogue but is insensitive to some extended NVSS sources (Becker et al., 1995).

1.4.3 VLSS

The VLA Low-frequency Sky Survey (VLSS) will ultimately cover the sky north of -30 deg declination at 74 MHz with 80 arcsec resolution and a rms noise of about 100 mJy (Cohen et al., 2007).

1.4.4 Cambridge Surveys

Source catalogues from the Cambridge 6C survey covering most of the extragalactic sky above +30 deg declination at 151 MHz with 4.2 arcmin X 4.2 arcmin * cosec (dec) resolution, (Baldwin et al., 1985). 7C survey covering most of the extragalactic sky above +20 deg declination at 151 MHz with 70 arcsec X 70 arcsec * cosec (dec) resolution (Hales et al., 2007). and the 8C survey covering the polar cap above +60 deg declination at 38 MHz with 4.5 arcmin X 4.5 arcmin * cosec (dec) resolution (Hales et al., 1995). All these surveys are relatively low frequency surveys and the survey being conducted with AMI for this thesis project is a much higher frequency survey at 15GHz.

1.5 The Need for High Frequency Radio Surveys

The majority of existing radio surveys have been conducted at the lower frequency end of the radio spectrum. However, there is also a need for radio surveys at higher frequencies. Surveys at frequencies at or below 1.4 GHz will miss objects whose spectra rise with frequency (Casassus et al., 2006). Examples of such objects include

HyperCompact HII (HCHII) regions and Anomalous Microwave Emission (AME)

(Watson et al., 2005). HCHII regions are believed to be the sites of the earliest visible stage of massive star formation. These regions are missed entirely by Galactic plane surveys concentrated at ν < 5 GHz (Tibbs et al., 2011) since low-frequency surveys preferentially select against dense plasmas. These plasmas are not limited to HCHII regions but also include a variety of other Galactic objects such as massive stellar winds, ionized jets from young stellar objects and young planetary nebulae (Scaife et al., 2009).

The mechanism for AME is believed to be emission from spinning dust, but many open questions remain and there is a need to provide more insights into the highfrequency Galactic plane through high sensitivity, resolution, and sky area coverage observations at these frequencies (Scaife et al., 2010). The reason for the lack of data to tackle these questions is that surveys of substantial areas of the sky at high radio frequencies are extremely challenging. Consequently, complete high radio frequency selected samples are rare and knowledge of the source population remains as a result poor.

1.6 The Challenge of High Frequency Radio Surveys

High frequency radio surveys (such as those above approximately equal to 10GHz) are highly time consuming and difficult to carry out (Davis, 2010). The scaling of interferometer primary beam areas with frequency, $\Omega \propto \nu^{-2}$ and the typical synchrotron spectra of radio sources, $S \propto \nu^{-0.7}$ result in the time required to carry out a survey of equivalent depth and sky coverage to scale as $t_{surv} \propto \nu^{3.4}$ (Davis, 2010; Thompson, Moran & Swenson, 2001). Furthermore, noise temperatures of the front-end, low-noise amplifiers used in interferometers also tend to increase with frequency, with $T_{LNA} \propto \nu$, and if this is a dominant component of T_{sys} then $t_{surv} \propto \nu^{4.4}$. Taken together, these effects mean that high-frequency radio surveys are much more time consuming than equivalent low-frequency radio surveys. For this reason, relatively little survey work has been undertaken at radio frequencies greater than 10 GHz.

1.7 Existing High Frequency Radio Surveys

There are exceptions of existing high radio surveys, such as the Ninth and Tenth

Cambridge (9C,10C) survey of radio sources (Waldram et al., 2003; Franzen et al., 2011) covering approximately 520 square degrees of sky at an observing frequency of 15.2 GHz and 27 square degrees at 15.7 GHz respectively. Significant survey work has also been carried out using the Australia Compact Array (ATCA) at 20 GHz (Massardi et al., 2008) to map the southern hemisphere of sky. There is yet to be a map completed for the northern hemisphere of sky at such a high frequency.

1.7.1 9C Survey

Waldram et al (Waldram et al., 2003) carried out the ninth Cambridge survey 9C of radio sources covering approximately 520 square degrees of sky at an observing frequency of 15.2 GHz using the Ryle Telescope (RT) (Pooley & Green, 1993) which has subsequently been upgraded to form the AMI LA. The prime motivation of this survey was to define a catalogue of the foreground sources monitored by the VSA during its observations of the CMB at a frequency of 34 GHz (Taylor et al., 2003) in order to remove their effects when conducting cosmological analyses. It is, however, of much wider interest, being the first survey covering an appreciable area at a radio frequency above the 4.8 GHz of the Green Bank survey (Gregory et al., 1996). In particular, it provides a means of identifying Gigahertz Peaked Spectrum (GPS) sources, which are important for the study of radio source evolution as well as being a significant foreground for CMB observations over a range of wavelengths (Waldram et al., 2003).

The RT is used for the observations was an East-West radio synthesis telescope. This E-W array of 5 aerials was spaced to give a resolution of 25 arcsec. 12 hours of data was combined into a single map used to identify peaks corresponding to possible radio sources. Each possible source was subsequently followed up with a short, pointed observation of 10 - 15 minutes either to establish a reliable flux density or else to eliminate it as a false detection.

1.7.2 10C Survey

The 10C survey observed an area of ≈ 27 deg^2 to an rms noise level of ≤0.2 mJy at 15.7 GHz, using the Arcminute Microkelvin Imager Large Array. These observations constitute the most sensitive radio-source survey of any extent (& 0.2 deg^2) above 1.4 GHz. The 10C source catalogue contains 1897 entries (Davies et al., 2010).

Comparisons of 9C and 10C surveys reveal contradictions in the AMI correlator which raised many data analysis problems. For instance, compared to the flux densities of the 10C survey, the 9C survey values were found to be small. Part of the problem was related to the inaccurate map scaling due to an error in the telescope’s RF frequency (Wright et al., 2009). This was corrected and resolved. Corrections were also applied to the bias resulting from phase errors due to uneven lag spacing in the correlator (Zottie et al., 2005). As a result of implementing these corrections, the origin flux densities were found to be in agreement with values calculated as part of the 9C survey over the typical flux density spectrum.

1.7.3 Green Bank Survey

Another survey is the Green Bank (GBT) survey which is the largest survey carried out at the highest frequency of 4.85 GHz. This northern sky survey was made with the former 91m telescope between 1986 and 1987. The final set of images covering the declination from 0 to 75 degrees was constructed with data from both epochs with 3 arcmin resolution. Its noise and position errors are nearly a factor of $\sqrt{2}$ smaller than in the epoch 1987 images, from which the 87GB catalogue of 54,579 sources stronger than S approximately equal to 25 mJy was extracted. The new images were used to make the GB6 catalogue of 75, 162 discrete sources with angular sizes less than 10.5 arcmin and flux densities above S approximately equal to 18 mJy at 6cm wavelength (Gregory et al., 1996).

1.7.4 Australia Telescope Compact Array Survey

Significant survey work has also been carried out using the Australia Telescope Compact Array (ATCA) at 20GHz (Massardi et al., 2008; Murphy et al., 2010; Ricci et al., 2004; Sadler et al., 2006) which has been used to survey the sky below declinations of -15 degrees to a (91 percent) completeness limit of 100mJY beam^{-1}. The catalogue of Murphy et al (Murphy et al., 2010) contains 5890 objects with flux densities greater than or equal to 40mJy (Corby et al., 2015)

1.8 Survey Techniques

1.8.1 Rastering Technique

The technique used in the 9C and 10C surveys is known as the rastering technique. This technique makes use of observations towards pointing directions lying on a 2D hexagonal lattice. The fields were observed with the lattice rows running along lines of constant declination. Since the RT is equatorially mounted, this is the natural way to observe in order to minimise time lost to slewing between pointings. Maps were created for each of the pointings and combined (Memon et al., 2000).

1.8.2 Drift Scanning Method

The rastering technique for this project would be extremely time consuming as hundreds of thousands of pointings would be required and overheads from telescope slewing and settling would make such a large survey of the whole of the northern sky impossible. Hence, a different method known as the drift scanning is employed, which utilises the movement of the sky as the Earth rotates. The telescope is held stationery and records data pointed at a fixed hour angle and declination and hence long strips at constant declination are observed. This drift-scanning technique is the method that will be used when imaging the entire northern-sky with AMI as this technique allows the scanning of large area surveys very efficiently. Ingalls et al., 2014)

1.9 The 11C Survey

The rest of this thesis describes work building towards the 11C survey, in particular studying how best to implement self-calibration. This survey will be conducted using the AMI-SA interferometer at 15 GHz in drift scan mode. The aim is to survey all of the northern sky to an rms flux sensitivity of 2mJy with a resolution of 3 arc-minutes.

Chapter 2 describes the process of radio interferometry.

Chapter 3 discusses the AMI telescope.

Chapter 4 details the data reduction pipeline for AMI observations, shows example maps and identifies imperfections in the images.

Chapter 5 explains the process of self-calibration, which aims to remove interferometric image imperfections.

Chapter 6 reports on the process of applying self-calibration to AMI drift scan data.

Chapter 7 provides a summary and discusses future work.

2 Interferometry

2.1 Introduction to Interferometry

The first radio interferometer dates back to 1946 when it was used by Ryle and Vonberg for the study of radio emissions from space that a few years earlier had been first discovered by Jansky, Reber and others. Interferometry is an important tool used in radio astronomy to achieve higher angular resolution in astronomical observations (Readhead & Wilkinson, 1978). Interferometry in radio astronomy is used primarily because it can achieve a much higher resolution than can be achieved with a single telescope (Cotton, 1979).

2.2 Single aperture telescopes

When a point source is observed, such as a star, with a telescope, a point image will not form on the focal plane since the circular aperture of the instrument causes diffracted rays to generate a particular “pattern” on the focal plane (Airy, 1835). These rings, which become increasingly weaker further away from the centre of the pattern, are the product of diffraction and have a peak in the central area, called the “Airy disk”.

The optical resolving power of a telescope is related to the size of the Airy disk which depends on the wavelength λ of the observed radiation and the aperture size D of the instrument. Using the approximation for small angles, Airy’s disc has an angular size given by the equation

$$\theta \approx 1.22 \frac{\lambda}{D} \tag{2.1}$$

the larger the diameter of the instrument, the greater the theoretical resolution.

Dividing by a conversion factor of 206,265 can convert radians to arcseconds, which is typically a more useful unit for the measurement of astronomical structures. Structures in nearby galaxies are a few arcseconds across whereas distant galaxies are approximately an arcsecond across (Neal, 2015). To increase a telescope’s resolution, for example to see things that are even closer to the centre of those galaxies, you will need to increase the frequency or the baseline length.

Early radio astronomy observations were conducted using single antennas but were significantly limited in their angular resolution of typically tens of arcminutes compared to traditional optical astronomy, which is of the order of an arcsecond (Lacy et al., 1995). Subsequently, at these poor resolutions, observations of a single radio antenna were insufficient for many astronomical purposes. This led to a problem where single dish astronomy struggled as larger and larger telescopes needed to be built to increase telescope resolutions, with the cost of the telescope rising with the cube of the dish diameter. This is illustrated by, for example, arcsecond resolution at $\lambda = 21$cm requiring $d = 43.3$ km; it is not possible to construct a single antenna of this diameter.

2.3 Interferometers

This problem can be overcome by using interferometry to increase the resolution. Since you cannot increase the size of an individual telescope beyond a certain point, instead lots of smaller telescopes which are a considerable distance apart are combined. Interferometry is the art of doing this in such a way that you produce an image which effectively synthesises a telescope with a physical size equal to the baseline distance between the multiple telescopes connected by links. The resolution of an interferometer is given by

$$\theta \approx \frac{\lambda}{B_{max}} \tag{2.2}$$

where B_{max} is the baseline length in metres.

Young's slits experiment can be used to explain interferometry. Young's slits experiment is an experimental set-up discovered by Thomas Young whereby a pair of slits is set-up and illuminated with coherent light. In order to get interference patterns, you need coherent light which is spatially and temporally coherent (Christiansen et al, 1985). Spatially coherent light means that the light has consistent smooth wavefronts i.e. they have constant phase relationship between each other and there are no corrugations in the wavefronts. Temporally coherent wavefronts mean are they coherent along the direction of travel of the wavefront i.e. the wave is monochromatic (Born et al., 1980). For example, lasers are very highly monochromatic sources of light. Different points can be taken across the wavefront giving a constant phase relationship between each point. If there is some sort of random corrugation in the wavefront then different points across a wavefront will not have a constant phase relation (Fried, 1965) which in fact can be a particular problem in radio interferometry.

Young's slit experiment is set-up so that the coherent light is shone on these slits towards a screen that is assumed to be at an infinite distance away from the slits. This generates an interference fringe pattern on the screen. The set-up is demonstrated in Figure 2.1. The interference fringes can be calculated from the two slits by considering the path difference between those two rays. If this distance, $Lsin\theta$, is an integer number of wavelengths, $n\lambda$, then the two rays interfere in phase when they arrive at the screen a very long way away. If it is $(n + \frac{1}{2})\ \lambda$ then the two rays will destructively interfere into nothing.

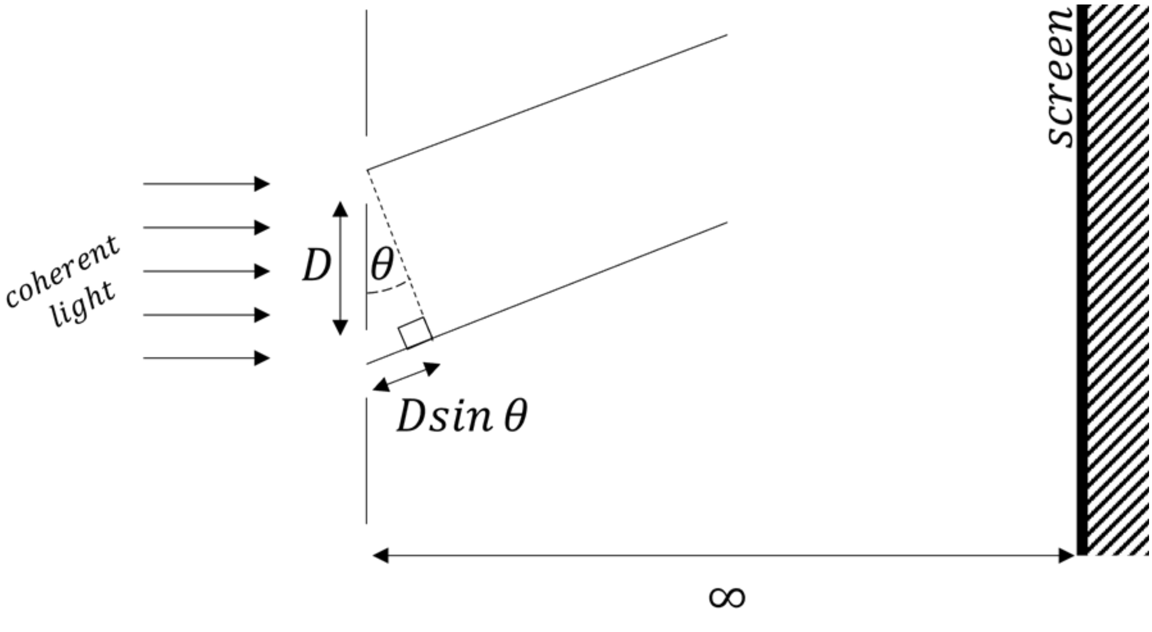

Figure 2.1 Young's slits

Therefore, in the small angle approximation, the angle between the first two bright points of constructive interference is given by $\theta \approx \frac{\lambda}{D}$. From this equation it can be seen that with a smaller slit separation then $\frac{\lambda}{D}$ increases, and so the angular resolution worsens.

We now extend this argument to consider a two element interferometer. Maximum light intensity is obtained when the angle θ formed by the direction of the source with respect to the optical axis of the instrument is such that the difference between the paths of the 2 beams is an integer number of wavelengths (Clark, 1981). If the angular dimensions of the source are small compared to the space between 2 adjacent interference maxima, the image of the source will be crossed by a clear pattern of alternating dark and light bands, known as interference fringes. Conversely, if the angular dimensions of the source are comparable to the spacing between the maxima, the image will be the result of the superposition of a series of patterns along the star, where the maxima and the minima of the fringes do not coincide, and the amplitude of the fringe will be attenuated (Yen, 1985).

The fringe visibility is defined as

$$\frac{I_{max}\;I_{min}}{I_{max}+I_{min}} \qquad (2.3)$$

where I is the intensity, hence I_{max} is the maximum intensity and I_{min} is the minimum intensity. The fringe visibility of an interferometer gives information about the Fourier transform of the sky brightness distribution (Jackson, 2019). In general, the visibility of the interference fringes decreases with increasing source size, going to zero when source size goes to $\frac{\lambda}{D}$. For a given source size, the visibility increases for decreasing separation but for a given source size and separation the visibility increases with λ. The correlation between source size and separation is represented in Figure 1.2.

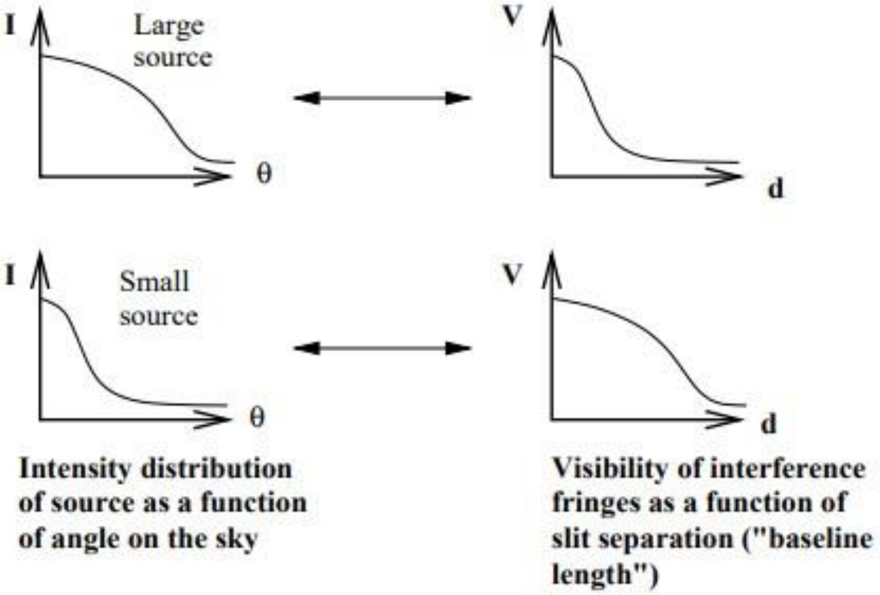

Figure 1.2: Relation between source brightness as a function of angular distance and visibility of interference fringes as a function of slit separation (baseline length). Ref: (Jackson, 2019).

The distributions in Figure 1.2 show a mathematical relation between the quantities whereby the small gaussian becomes a big gaussian and vice-versa. This relation represents a FT i.e. the relationship between brightness as a function of angle and the fringe visibility of the resulting interference pattern as a function of baseline is a FT. This demonstrates that long baselines give information about the small scale structure of the source but are insensitive to large scale structure. Similarly short baselines give information about the large scale structure but are insensitive to the small scale structure of the source that is the resolution of the source.

In summary a signal from space arrives at each antenna at a slightly different time (due to different path lengths) depending on the location of the antenna in the array. The signals arriving from slightly different points in the sky arrive at slightly different times at each antenna. This provides location information within the telescope beam and thus positional information about the emitting object. The signal from each antenna is then combined with every other antenna in a correlator, where the time delay is measured and compensated for in the software.

2.4 Visibilities

Interferometers measure visibilities, which are the amplitude and phase information of the cross-correlated signals between pairs of antennas. The data is calibrated by determining the complex gains (amplitude and phase) and the frequency response (bandpass) for each antenna. The complex visibility measured by a radio interferometer is a single Fourier component of the sky brightness distribution, so a map of the sky can be made by using Fourier synthesis to combine measurements obtained with different interferometer baselines (Rudelson et al., 2006). This technique is known as aperture synthesis. A common problem in aperture synthesis is that the phase of the complex visibility is badly corrupted by instrumental and propagation effects. Over short baselines, such as the AMI Small Array baselines, these problems can generally be overcome by careful calibration of the instrument using observations of unresolved sources.

2.5 The u, v plane

The u, v plane is effectively the decomposition of the projected baseline vector drawn between two telescopes as shown in Figure 2.3. This vector is then decomposed in terms of a North-South component and an East-West component shown in Figure 2.4.

The equations for u and v are given by the following

$$u = \frac{L}{\lambda} \cos d \sin(H - h) \tag{2.4}$$

$$v = \frac{L}{\lambda} (\sin d \cos D - \cos d \sin D \cos(H - h)) \tag{2.5}$$

where D is the declination of the source, d is the declination of a point on the sky pointed to by the baseline, H is the hour angle of the source and h is the hour angle of the baseline. The baseline vector is decomposed into two components: one parallel to the equator at its nearest point to the source, and the other as parallel to the line between this point and the north pole. Figure 2.3 shows how the projected baseline vector appears as a line drawn on the earth if taken from the perspective of the source. (Jackson, 2020)

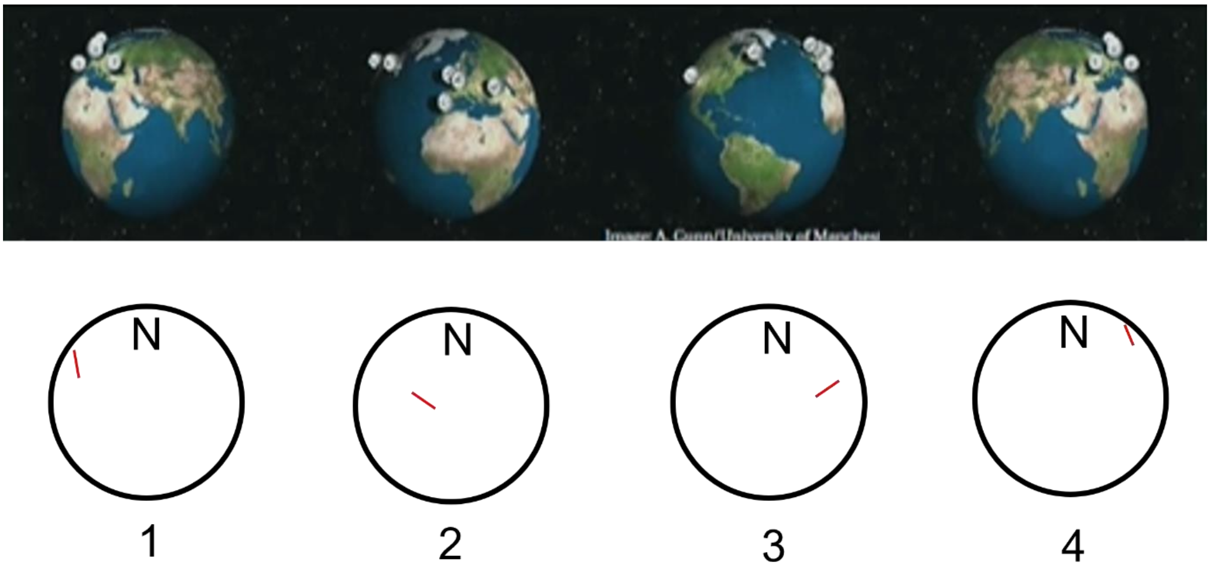

Figure 2.3: Earth rotation and observing baseline. Ref: (Grainge & Scaife, 2019)

As the earth rotates it can be seen that the components trace out an ellipse in u, v space during one earth rotation (Jackson, 2020). Due to the rotation of the Earth, over time any pair of telescopes will have a baseline vector which has changed both in length and orientation. This is very useful to radio astronomy, since a single baseline can sample the interferometer response function at lots of different points meaning better information about the structure of the source can be obtained than would be achieved from a single snapshot observation. In this case, the projected baseline vector is resolved into a North-South and East-West component giving a position each time it is resolved, on the diagram. Hence, from position 1 to 2 to 3 to 4 it can be seen that the baseline vector has traversed from one point in the u, v plane to a completely different point in the u, v plane. As the interferometer response function as a function of u and v is the FT of the sky brightness distribution of the source then it follows that by measuring the interferometer response function at every single point in the u, v plane and applying a FT would give an image of the source.

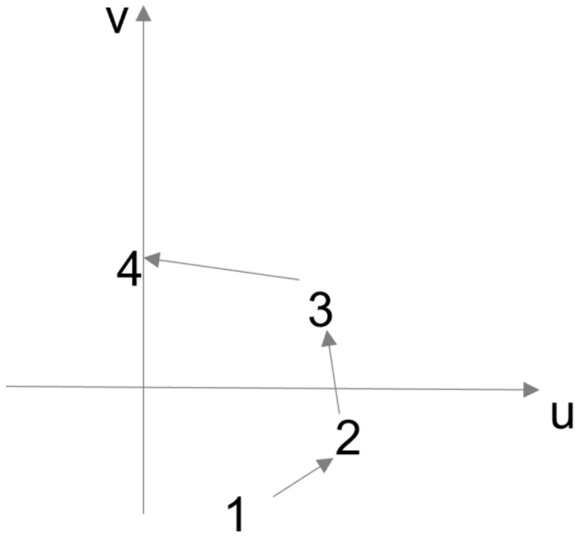

Figure 2.4 Earth rotation in the u,v plane. The numbers 1-4 correspond to the numbers

in the previous Figure, Fig. 2.3. Ref: (Grainge & Scaife, 2019).

However, a limitation on imaging is placed due to the fact that the interferometer response function cannot be measured over the whole u, v plane. The result of this incomplete u, v plane sampling is that Fourier transforming the measured visibilities results in the production of what is called the dirty map.

The exact form of u, v tracks can be demonstrated using Figure 2.5. The clumps of points show visibilities associated with the each of the 45 different baselines. Within each clump, the extended arcs are caused by the change in projected baseline during the course of the 1 hour run due to Earth's rotation. Also visible are six radially distributed arcs which are due to the different frequency sub-bands observed by AMI.

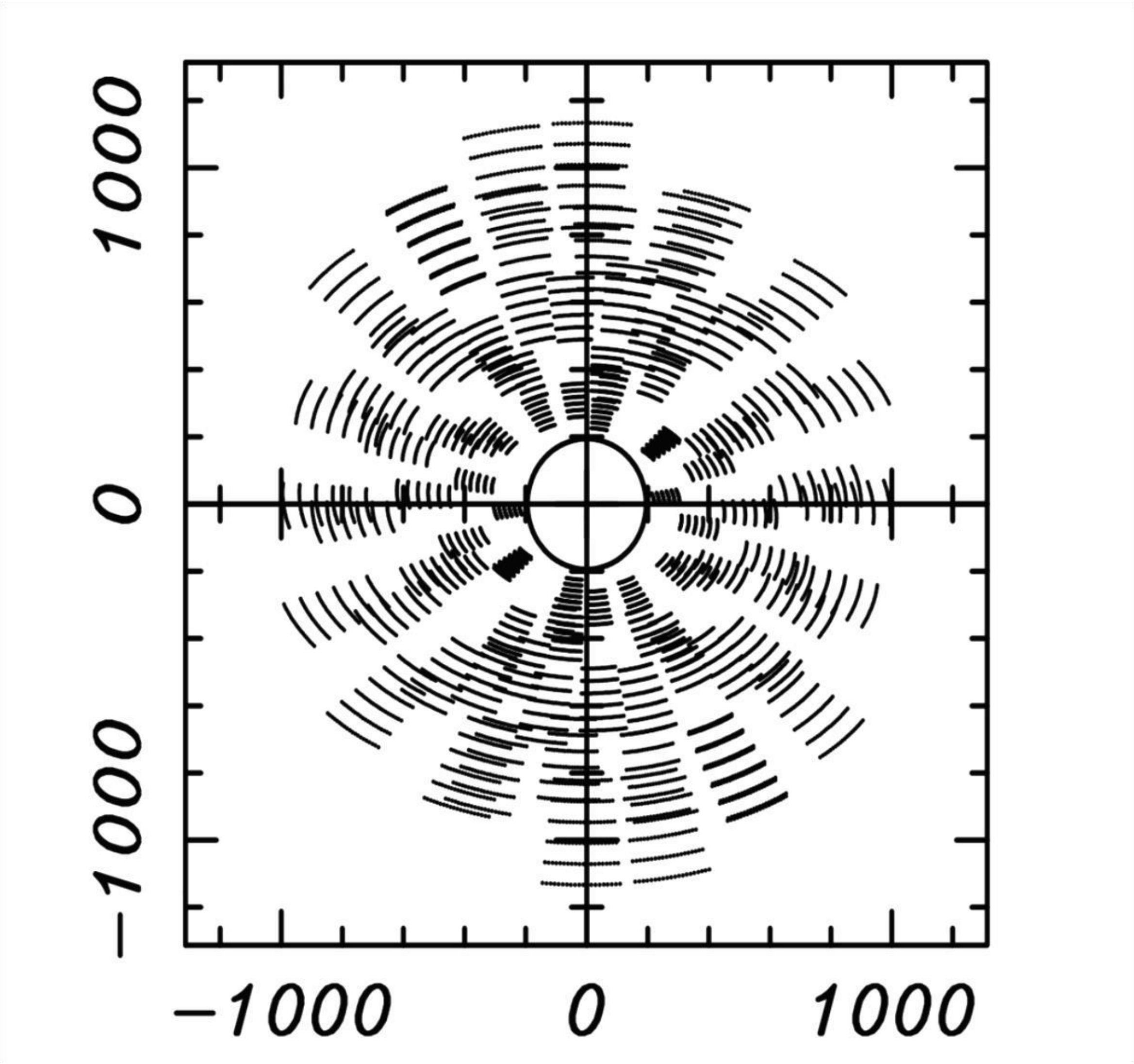

Figure2.5: Simulated uv-coverage of a one hour AMI Small Array observation towards

a field at Dec = 30. Ref: (Jackson, 2019)

2.6 The Dirty map

This problem can be summarised through wanting the image $I(x, y)$

resulting from the full u, v response function

$$I(x, y) = \int \int V(u, v) e^{i2\pi(ux+vy)} du dv \tag{2.6}$$

but instead having the "dirty image"

$$I_D(x, y) = \int \int V(u, v) S(u, v) e^{i2\pi(ux+vy)} du dv \quad (2.7)$$

where the sampling function $S(u, v)$ is 1 in parts of the u, v plane which are measured by the interferometer and 0 otherwise, i.e.

$$S(u, v)_{coverage} \quad \times \quad V(u, v)_{true} = V(u, v)_{measured} \quad (2.8)$$

Since the right-hand side of Equation 11 is a FT, where the argument is the product of two functions I and S, the convolution theorem can subsequently be used to re-write the equation as

$$I_{dirty}(x, y) = I(x, y) * B(x, y) \quad (2.9)$$

where

$$B(x, y) = \iint S(u, v) e^{2\pi i(ux+vy)} du dv \quad (2.10)$$

is the “dirty beam”, which is the FT of the sampling function. The dirty beam is therefore the interferometric point-spread-function (PSF), meaning that the dirty map is the true sky brightness distribution convolved with the dirty beam. Recovering the image $I(x, y)$ is therefore a classical deconvolution problem (Frater et al., 1980).

2.7 CLEAN

The CLEANing technique can be used to deconvolve the effect of the dirty beam from the observed brightness to give the true brightness of the source and was developed by Högbom in 1974 (Högbom, 1974). The method works by shifting the dirty beam to the brightest source in the dirty map. The dirty beam is then scaled and subtracted off using a given amplitude multiplied by the brightest source value (Schwarz, 1978). The subtractions are repeated until the residual map from which the dirty beams have been subtracted consists solely of noise (Clark, 1980). A final CLEAN map is produced by the convolution of the subtracted fluxes with a Gaussian (fitted to the centre of the dirty beam). (Pearson & Readhead, 1984).

As the recorded visibility data is not uniformly distributed across the u,v plane and is usually concentrated towards the centre (Cornwell, 1982), data weighting must be taken into consideration. Weighting can be applied through “natural weighting” which treats all the data points equally or “statistical weighting” treating all the data points with the relevant weightings (Schwarz, 1978) or “uniform weighting” which applies equal weights to each region of the uv grid. Uniform weighting results in a dirty beam with lower sidelobes, which will make the CLEANing process more robust, though there is a loss in overall signal to noise.

The additional information that has been supplied to the deconvolution problem by CLEAN is the assumption that the sky consists of a finite number of point sources (Tan, 1986). Subsequently, CLEAN works well for straightforward point-like sources, but can sometimes fail on very larger undefined sources with faint surface brightness (Cornwell, 1982).

2.8 Atmospheric Corruption

The radio signal from a source travels as a pretty perfect plane wave, and unfortunately in the last few milliseconds of its travel it goes through the atmosphere. Passing through the atmosphere turns the signal from a plane wave into a corrugated wavefront. These corrugations introduced in the atmosphere vary both with position and time. This is a serious problem as can be understood from the analogy with Young’s slits, where the derivation of the interference pattern relied upon the wavefront being coherent.

Different regions of the Earth’s atmosphere introduce different corruptions to the radio signal. The ionosphere corrupts wavelengths at low radio frequencies (typically a few hundred MHz) and this effect is typically most problematic at times of solar maximum as it responds to solar activity. At AMI’s observing frequency of 15 GHz, the effect of the ionosphere is negligible, and the dominant corruption occurs in the troposphere (Armstrong et al., 1982).

The troposphere of the earth introduces phase changes due to the amount of water vapour and oxygen that the radio waves need to travel through (Barrett et al., 1982). The atmosphere is constantly changing which means the phase that the telescope will measure from a bright source will also change. There is also a time varying amplitude due to things like different amounts of absorption. These both result in amplitude and phase errors on the correlated signal between pairs of antennas (Barrett et al., 1982).

2.9 Interleaved Calibration

To remove these errors, the telescope can be pointed at a known point-like source. The theoretical interferometer response from such an observation can be calculated and any differences between this and the measured visibilities can be ascribed as being due to the effect of the atmosphere. This gives a measure of the phase introduced by the atmosphere. Observations of the field of interest are interleaved with periodic observations of the bright source then it becomes possible to calibrate away the corrupting effect of the atmosphere.

The measured atmospheric phases on the bright calibrator source can be linearly interpolated and subtracted from the phases of the visibilities towards the field (Bieging et al., 1984). The calibrator source has to be close in position to the field being observed, so that the atmosphere towards the calibrator is roughly the same as the atmosphere towards the field. This has to be done for every single baseline and every single frequency channel. Therefore, interleaved calibration effectively takes out the phase introduced by the atmosphere. A similar method can be applied to the amplitude calibration by accounting for any changes between the model and the amplitude actually received.

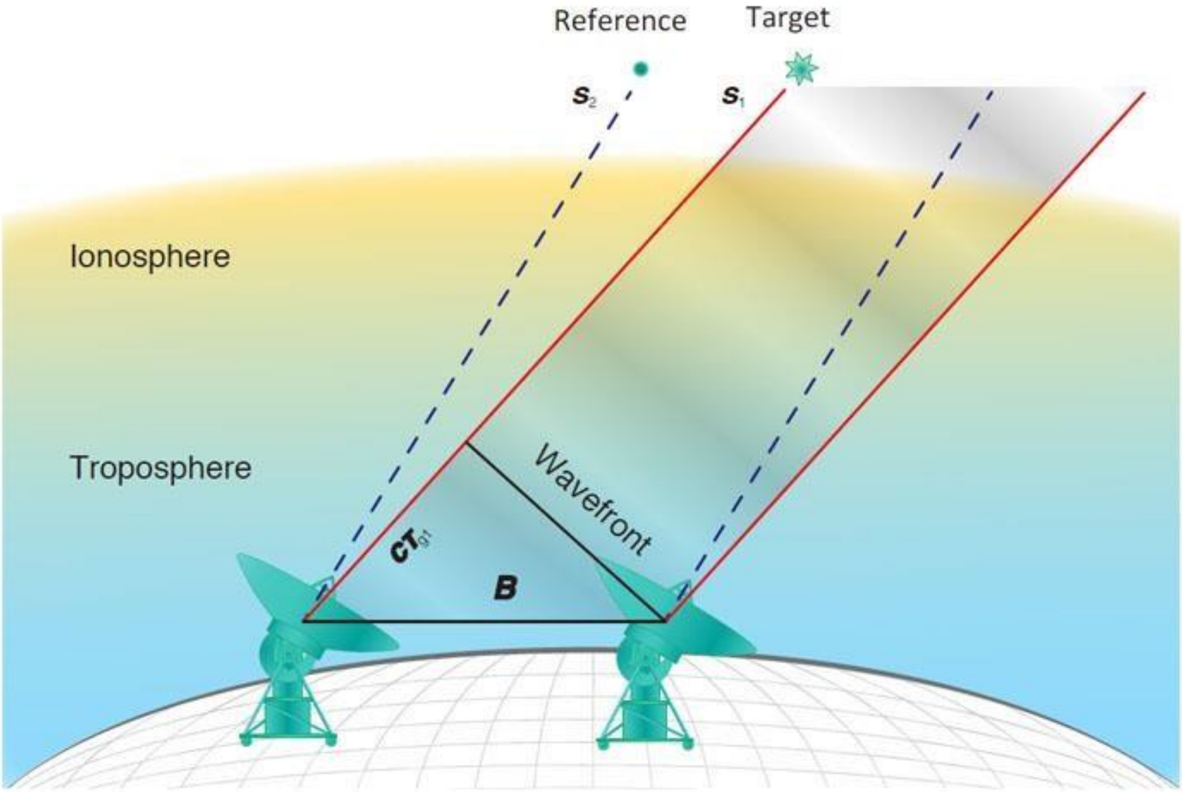

Figure 2.6: Schematic view of a delay measurement in phase-referencing astrometry.

Credit: https://ned.ipac.caltech.edu/level5/March14/Reid/Reid4.html

Figure 2.6 shows an array with two antennas, which is used as an example for simplicity. The baseline vector and source directions are indicated by lines. In relative astrometry, the target and adjacent reference sources are observed at the same time so delay errors can be effectively cancelled in the relative measurement (Madore et al., 2020).

For the majority of the observations taken for the AMI drift scan survey, interleaved calibration is a useful procedure and these errors do not result in noticeable degradation of the image quality. However, in a field that contains a bright source, these uncompensated errors cause artefacts to appear in the map, degrading image quality. Removing these artefacts is the motivation for employing self-calibration which is the focus of chapter 5.

2.10 Closure Quantities

Closure quantities can be used to recover the information from badly corrupted visibilities using a minimum of three antennas simultaneously (Chael, 2018). Mapping is then possible in the presence of large systematic errors in both the amplitude and the phase of the measured visibilities. These mapping methods, self-calibration, or hybrid-mapping, make use of the fact that it is possible to form combinations of the measured visibilities called closure phases and closure amplitudes that are independent of such errors (Pearson et al., 1984). This partial phase and amplitude information is then used together with the constraint that the source brightness distribution is positive to retrieve the full visibility information and as a result generate reliable images.

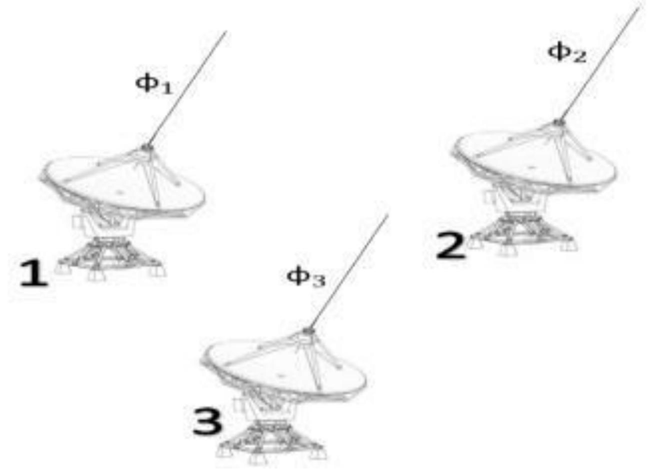

Figure 2.7: telescope set-up of 3 arrays

Consider the atmospheric phase based errors (Battat et al., 2004) associated with each of the antennas where the phase error on antenna i is represented as Φ_i, then the visibilities formed from correlating a triangle of three telescopes as shown in Figure 2.7 will obtain three phase responses containing the phase error terms Ψ_{12}, Ψ_{23}, Ψ_{31} defined as

$$\Psi_{12} = \Phi_2 - \Phi_1 \tag{2.11}$$

$$\Psi_{23} = \Phi_3 - \Phi_2 \tag{2.12}$$

$$\Psi_{31} = \Phi_1 - \Phi_3 \tag{2.13}$$

and adding those together gives

$$\Psi_{12} + \Psi_{23} + \Psi_{31} = 0 \tag{2.14}$$

Since these error terms sum to zero, then summing the phases of measured visibilities from a triangle of antennas leaves only information on the astronomical structure. Modelling these “closure phases” can obtain constraints on the phases of the response function in the u, v plane and hence allow the source structure to be deduced.

3 The Arcminute MicroKelvin Imager

The observations analysed for this project are carried out by the Arcminute Microkelvin Imager (AMI). AMI is a radio interferometer located in Cambridge and operated by the Cavendish Cambridge group. The current primary aims of AMI are to observe secondary anisotropies in the Cosmic Microwave Background (CMB) and the effects caused by the clustering of galaxies known as the Sunyaev-Zel'dovich (SZ) effect as discussed in Kneissl et al., 2001, although this is not something that will be looked into further throughout this thesis.

3.1 Upgrades in AMI Correlator

There has been recently a digital correlator upgrade for AMI. The original correlator recorded visibilities in eight frequency channels over AMI's 12-18GHz band giving limited capability for recognising and removing interfering signals as well as limited ability to mitigate chromatic aberration out to the edge of the field of view (Hickish et al., 2018). Hence, the sensitivity of observations was significantly reduced particularly at low declinations where interference from geostationary satellites could result in up to 90 percent of the data being unusable (Hickish et al., 2018).

3.2 Array Design

3.2.1 Number and Size of Antennas

AMI is made up of a pair of interferometer arrays of which operates six frequency channels spanning 13.9–18.2 GHz, for observations on angular scales of 30 arcsec to 10 arcmin and for declinations greater than −15 degrees (Zwart, 2008). AMI observes in one linear polarisation, therefore measures Stokes’ I+Q.

Figure 3.1: LA from the north-east. The correlator is in the central hut. The railway track, which runs diagonally across the photograph, is approximately east-west. Four antennas are moveable along the track. Ref: (Zwart et al., 2008).

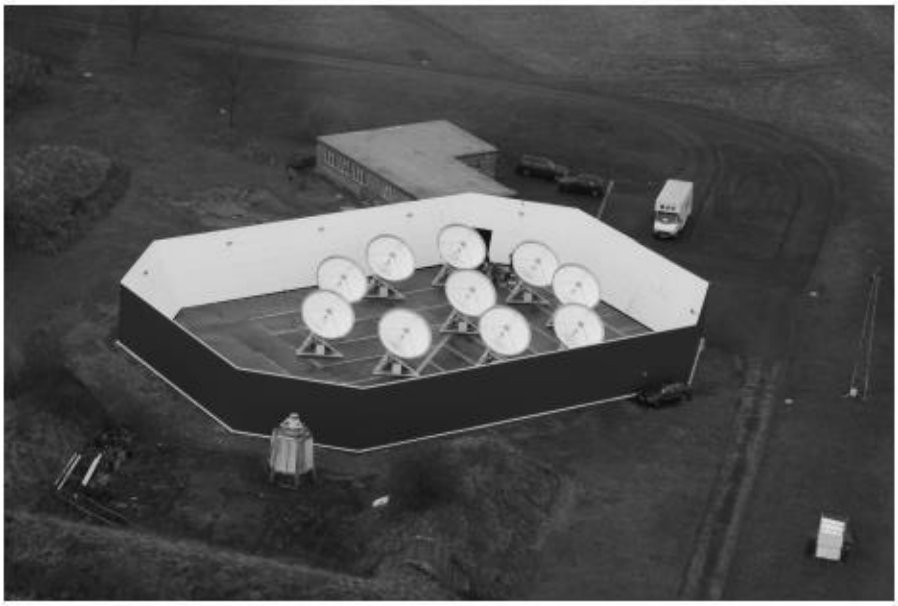

Figure 3.2: SA from the south-east. the correlator is in the building behind. The enclosure floor is covered in aluminium. Ref: (Zwart et al., 2008).

AMI, made up of two interferometers, is known as a twin-array radio telescope system. The interferometers are called the Small Array (SA; Figure 3.1) and the Large Array (LA; Figure 3.2). The SA has a sensitivity of 30 mJy $s^{-\frac{1}{2}}$ and the LA has a sensitivity of 3 mJy $s^{-\frac{1}{2}}$. (Zwart, 2008). The SA is optimised for observing extended SZ decrements on arcminute scales and works in conjunction with the LA which operates at a higher resolution and subsequently is used to characterise and subtract point source foreground data from the SA data. Implementation of such a method by the LA can be used as a calibration accuracy check for data obtained by the SA.

The AMI SA, which will be used for observations of this project, has 10 antennas labelled for the purpose of this thesis, 1 up to 10. The design of one of these antennae is shown in Figure 3.3. Typically for an array of antennas, all pairs of these antennas are cross correlated which will give 45 visibilities. The SA ten dishes are each 3.7m diameter with a range of baselines of 5 – 20m operating at a frequency of 13 – 18GHz. The configuration of the SA is shown in Figure 3.4. The LA comprises of eight 12.8m diameter dishes with baselines in varying length of 17 – 107 metres and it operates at the same frequency span. The configuration of the LA is shown in Figure 3.5.

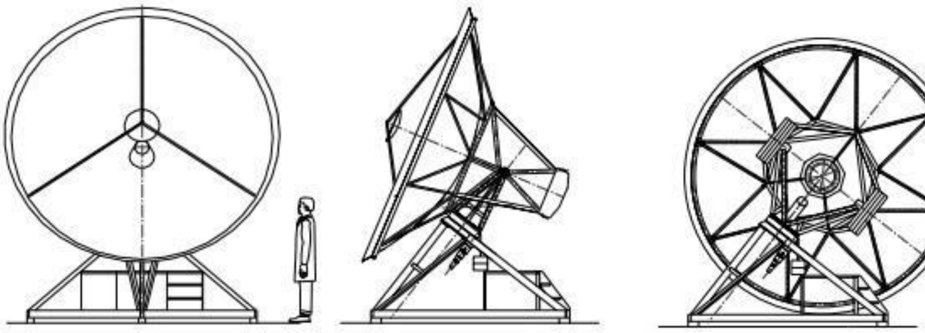

Figure 3.3: A single SA antenna. Ref: (Zwart et al., 2008).

Multiple antennas such as the one shown in Figure 3.3 are generally expensive to build because of the costs associated of the electronics and correlator required per antenna (Huang, Guo & Rao, 2018). However, this has to be balanced against the cost of each antenna, which rises with the cube of the antenna diameter (Cornwell & Wilkinson, 1981).

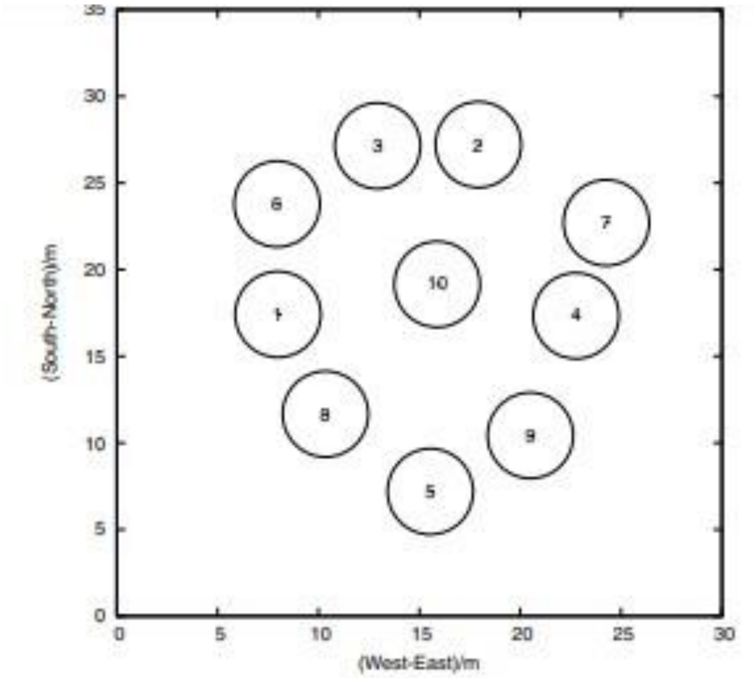

Figure 3.4: Current SA relative antenna positions in metres (Zwart et al., 2008).

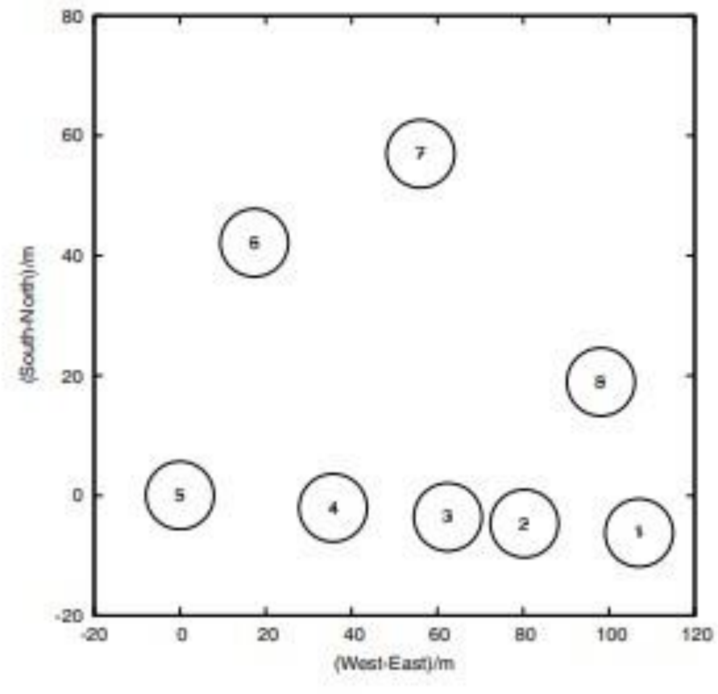

Figure 3.5: LA relative antenna positions in metres (Zwart et al., 2008).

The 11C survey is observing sources which are typically small compared with the synthesised beam. The AMI array is set up in such a way that is ideal due to its twin array system particularly because the LA has a greater diameter, but fewer antennas and the SA has a smaller diameter of antenna but more antennas meaning a survey can be carried out by the smaller array and followed up at a higher resolution by the larger array.

3.2.2 Signal-to-Noise Ratio

A high Signal-to-Noise Ratio (SNR) is of course desirable for the survey. To generate the best SNR for the telescope, the greatest signal and least background noise is needed (Kneissl et al., 2001). Signal is proportional to the effective area A_e of the telescope. Noise, which is the total random contribution from various background sources which affect signal measurements (Ko, 1964), can also be described in terms of temperature. In the case of the AMI telescope, the system temp T_{sys} is a measure of the total noise level (Boone, 2001).

The system temperature needs to be minimised to minimise the telescope noise. The system temperature is made up of the total receiver temperature T_R, which represents the internal noise from the receiver components (Reid, 2006), plus the unwanted noise incurred from connecting the receiver to the antenna and from the noise components from the antenna produced by ground radiation, atmospheric emission, ohmic losses, and other sources. (Taylor et al. 1999). The system temperature of the AMI-SA is approximately 25K.

3.2.3 Sensitivity

To conduct large area surveys, imaging of multiple pointings is required (Hopkins & Beacom, 2006). The primary beam size is given by $\frac{\lambda}{D}$ and so the number of pointings required to cover a region of the sky will be proportional to D^2. The flux sensitivity ΔS_{rms} of an array consisting of n antennas each with effective area A, integrating for a time τ, measuring a single polarization with bandwidth $\Delta \upsilon$ is given by

$$\Delta S_{rms} = \frac{2kT_{sys}}{\eta A[n(n-1)\Delta\nu\tau]^{\frac{1}{2}}} \tag{3.1}$$

where η is the system efficiency, T_{sys} is the system temperature (assumed to be the same for each antenna) and k is the Boltzmann constant (Thompson, Moran & Swenson 1986). This shows that best sampling times are achieved with a larger collection area of the telescope as the imaging sensitivity is proportional to nD^2 (Prandoni et al., 2015).

4 The AMI Data Reduction Pipeline

The 11C survey covers an area of 20,000 square degrees of sky, with a total observing time of over a year (note that the AMI-SA conducts a wide range of observations and also that observations were disrupted due to the Covid-19 pandemic). Tens of thousands of individual maps will need to be imaged, and so an automated data reduction pipeline is essential. The individual maps then need to be combined together in a weighted fashion that takes into account the noise level in the component maps. Source finding then has to be run over the combined maps. Accounting for all considerations of SNRs, a useful detection threshold can be defined as a SNR of 5 (Hainaut, 2005). This means that detecting source flux density of 10 mJy requires a maximum noise level of 2 mJy.

4.1 Pipeline Summary

AMI drift scan observations have a typical duration of several hours and so map out a strip of sky several tens of degrees in width in Right Ascension (RA), while the Declination range is determined by the AMI-SA primary beam of 20 arcminutes FWHM. Bright calibrator sources are observed every 30 minutes. Individual maps spaced 10 arcminutes apart in RA are made. Since the sky drift rate is $\frac{15}{\cos D}$ arcseconds per second, the amount of data that goes into an individual map is typically around 40-60s. First individual maps are made using interleaved calibration, sources bright enough for self cal are identified, and the inputs for a model (ie RA, Dec and flux) are extracted from the data. Starting from visibility data for a pointing (~40s of data) which has had interleaved calibration applied, a model based upon the source model and a Gaussian approximation to the primary beam is added to the visibility dataset (the MODEL_DATA column in the CASA ms). Antenna based gain corrections are derived from an over-constrained set of simultaneous equations (one per baseline) comparing the measured visibility with that from a time and frequency resolved model.

Then, to image, the model is subtracted from the self-calibrated data. The subtracted visibility dataset is cleaned (ie any residual flux after subtracting the model and/or other sources too faint to appear in the model are cleaned). The source model is added back into the map plane as a point source convolved with a Gaussian approximation to the inner part of the synthesized beam

4.1.1 Terminology

The calibrators are listed such as 3C-. The timestream data sets are listed as DJ-. The large maps are listed as J. More terminology can be found in the glossary at the end of the thesis.

4.2 Pipeline Set-Up

Many of the methods discussed in the literature review were considered for use in this research project. The suitability of the calibration approach used depends upon the specific conditions of the data to be explored. Many factors have an important impact upon the calibration including weather, atmospheric conditions, observing frequency, location, antenna size and array size of the interferometer, surrounding artefacts altering the visibility of the data. The initial calibration pipeline description is described in detail below.

The AMI git repositories need to be copied into the user's home directory. The correct directories in the terminal where some of the data output will get processed to from running the scripts are demonstrated in Figure 4.1. The main script is the run_drift.py script and inside this script the modifications of the paths 'git_path', 'fitsidi_dir', 'data_dir', 'SWarp' need to be changed to the user relevant directories.

A directory called casa contains all the casa master tasks and python scripts so that the script finds everything. These are subdirectories inside the 'data_dir' directory where the output files from the script will be organised and need to be created before running the script. After these paths are set, the variables 'profile' and 'pipepath' are set based on them.

The 'pcals.list' file is a list of primary calibration observations matched to the drift scan observations and is needed for running the CASA version of the pipeline. For the running of the quicklook data (referred to as quicklook mode), the 11C_00_00 folder contains the relevant source lists, whereas the 'all.list' file produced from the running of these source list is the one used for the CASA pipeline (referred to as CASA mode).

4.3 Quick Look Mode

Quick look mode runs 'reduce_dc' to calibrate the quick-look data, producing the uvfits files then make the casa image runfile script for imaging them in CASA and the wrapper script for running the imaging and running SWarp to combine them. The main output of the quick-look reduction is the first-pass source list to use in the CASA reduction (the all.list file) produced for each patch of sky. The observation list is used to calibrate and an additional source list producing final maps. Then this generates the reduced quick-look data for the observations and produces the uvfits files that will be used to input into the CASA run mode.

4.4 CASA Mode

Running CASA mode produces the reduction runfiles and subsequently produces a wrapper shell script. This shell script is used to run the first reduction script for all the observations, then fit for fluxes and spectral indices of the bright sources in the uvplane, then run the second reduction script which performs some extra amplitude self-calibration based on the results of the uv-plane fitting.

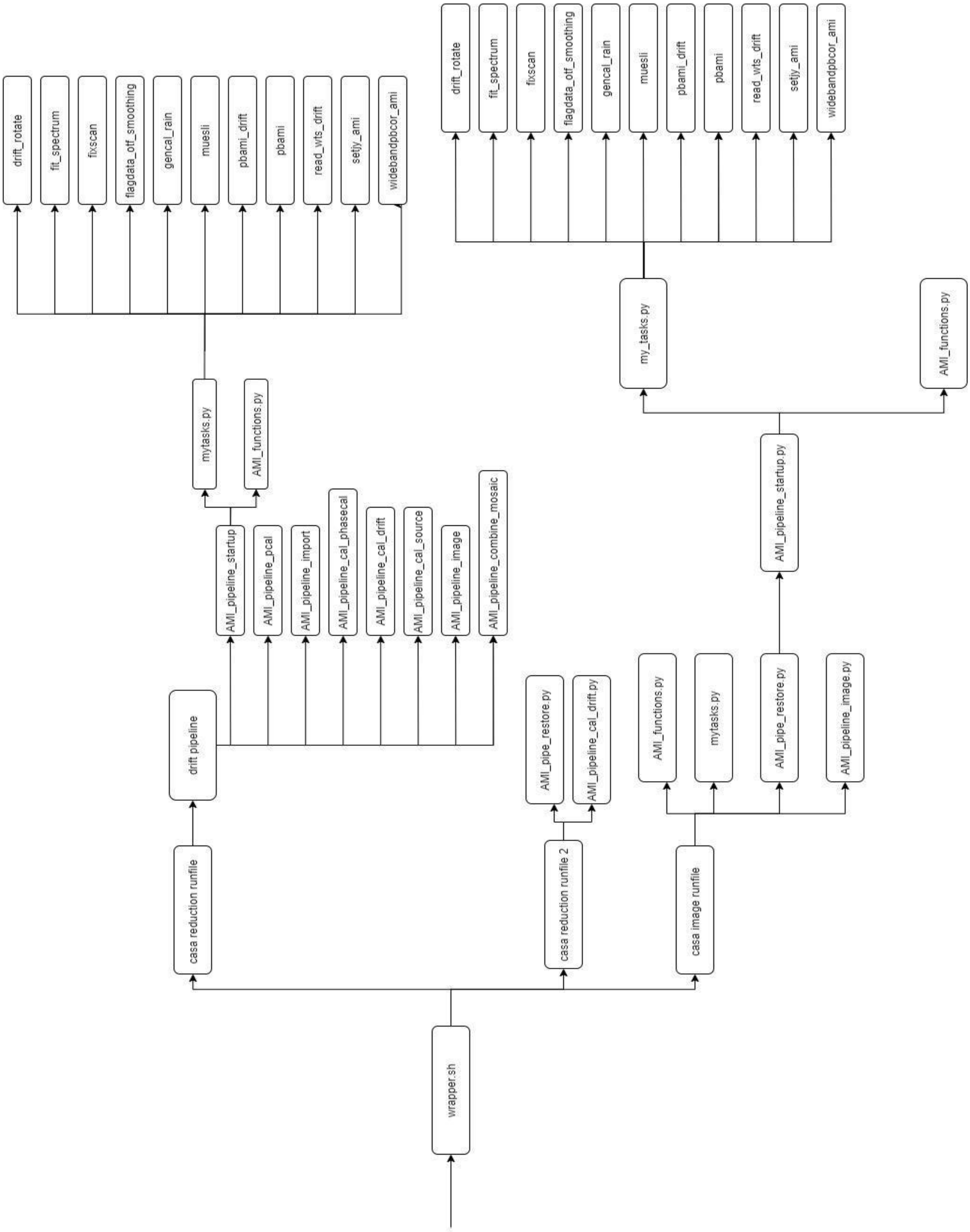

Figure 4.1: Flow diagram showing the various steps of the AMI data reduction pipeline The following process is how the maps are made. Firstly, there is a source list used to make a quick look reduction of the

data and this is input and then from this the quick look maps are made which are used for the self-calibration process. The array used is the Small Array and it is processed using CASA and output mapsize of 7.0 arcmin by 6.8 arcmin. SWarp is run on these initial maps as well to produce the strips.

From this run 3 other python scripts are produced, the CASA Reduction Runfile 1 and 2 and CASA Image Runfile. A wrapper script is also produced which is what is used to perform the reductions of the python scripts on the measurement sources.

The list of drift scan files to process asks for the list of observations i.e. this file contains the list of observation names that are reduced, one per line, with or without the .raw extension. Following on from this, the same observation list file is used but an additional source list (all.list), which is a list of all the sources detected in the initial quick-look maps. The map size is also slightly bigger than the default, just to accommodate the dimensions of the patch better.

4.3.1 Wrapper Script (wrapper.sh)

The wrapper script is created from running the CASA mode version of the pipeline. This script will perform the imaging of the individual pointings, primary-beam-correct them and output as FITS for input to SWarp. The CASA map files are generally removed but can be kept by setting remove maps=False in run drift.py which is useful during debugging and when running imaging tests; merge catalogues.py is used during the mapping step to average the fluxes of bright sources which have been observed in multiple observations before re-adding to the maps.

4.3.2 Step 1: CASA Reduction Runfile

The CASA reduction runfile script sets some paths and then runs a standard drift pipeline script from the git repository. This script uses the primary calibration observation to get phase and amplitude bandpass solutions, applies these to the observation, makes phase calibration solutions using the interleaved calibrator, and interpolates them onto the science field, while doing interference flagging along the way.

This script should be run with the inputs for the calibration observation and the observation source and outputs the DJ000-..... folders in the data reduction directory containing the reduction. Inside these folders a reduced ms, some calibration tables and some output diagnostic plots are produced. The CASA reduction runfile script contains the drift pipeline which contains:

4.3.2.1 AMI_pipeline_startup

This pipeline is used to set up some array-dependent calibration parameters. These parameters may need some experimentation and tweaking for individual observations. Note that on restarts the saved parameters were overridden with the default ones so it was important to check this every time when making edits to the calibration parameters that were tweaked during the research.

4.3.2.2 AMI_pipeline_pcal

This script was used to make primary calibration tables. These plots can be looked at made from the primary calibration observation in a folder which contains these diagnostic plots.

4.3.2.3 AMI_pipeline_import

This script was used to import the science observation, do initial flagging and get the source information.

4.3.2.4 AMI_pipeline_cal_phasecal

This script was used to calibrate the phase calibrator in a science observation which could either be the interleaved calibrator or the source itself. For this, to flag the interleaved calibrator effectively without biasing the amplitude, a model was calibrated so that the residuals can be flagged. If self-calibration was being performed, which in this case it was, then a separate manual setting of selfcal flagging, in which case all sources should be treated both as calibrators and sources was used in the script. Within this section of the script the solution interval was changed for different methods of self-calibration techniques.

4.3.2.5 AMI_pipeline_cal_drift

This script performed the calibration of an AMI drift scan observation. Calibrate an AMI drift scan observation. Flag the calibrated field data, assuming it's noisedominated. Apply calibrations (including rain gauge which is a system for real-time monitoring of the system temperature through the injection of the signal from a noise diode modulated at around 1 kHz into the receiver so the source model can be used). The first step of the calibration looks for interference localized in both time and frequency, then looks for broad-band interference. Custom on-the-fly smoothing flagging is performed.

The plotted calibrated data is then split out and binned down to 128-channel bins for imaging. It’s then reweighted using scatter of visibilities at each point in time, and the frequency information after the split. Phase rotation to drift scan pointing centres is performed on the data and then self-calibration in phase or phase and amp is tried. Within this pointings with <50% unflagged solutions are removed from the dataset. For the rest of the data, it is imaged and the subtracted data and then the sources are added back in the map plane.

4.3.2.6 AMI_pipeline_cal_source

Calibrate the source in an AMI observation, if not self-calibrated.

4.3.2.7 AMI_pipeline_image

Images the source only.

4.3.2.8 AMI_pipeline_combine_mosaic

Combine together individual pointing centre maps into a mosaic, using the noise estimates for weights.

4.3.3 Step 2: u, v Plane PS Fitter

The script uvplane_ps_fitter.py which fits a flux density and spectral index for the brightest sources detected in each declination strip, in the uv-plane using the fits file output from the initial CASA reduction script and creates an updated source list to use in the next reduction script. The important thing is that chains/DJ0000+0013180707_8.list_add_spec is output. This is the updated source list with the parameters as fit by uvplane_ps_fitter.py. DJ0000+0013_8.ms and DJ0000+0013_8_sub.ms is outputted into the fitsidi/DJ0000+0013-180707/ folder.

4.3.4 Step 3: CASA Reduction Runfile 2

The CASA Reduction Runfile 2 script contains:

4.3.4.1 'AMI_pipe_restore.py'

This is a script that restores all variables needed by the AMI pipeline into the global namespace and is adapted from the EVLA pipeline. For this script, 'startup' is run to load all the functions and modules needed for the pipeline which then restores all the variables to the global namespace. The pipeline_restore script has to be recalled before and after the startup to firstly declare some variables used in AMI_pipeline_startup.py, then afterwards restore the saved parameters overridden by the defaults.

4.3.4.2
‘AMI_pipeline_cal_drift.py’

Same as above.

4.3.5 Step 4: CASA Image Runfile

The CASA Image Runfile 2 script contains:

4.3.5.1 'AMI_functions'

This script contains the functions used for running the AMI pipeline.

4.3.5.2 'AMI_pipe_restore'

AMI_pipeline_restore contains all the AMI tasks and functions needed to restore the pipeline to its original state. The scripts contained within this pipeline section were generated using xslt from its XML file and Copyright 2009, Associated Universities Inc., Washington DC. The scripts are:

4.3.5.3 'DRIFT ROTATE'

This script phase rotates drift scan data to pointing centres for example, drift_rotate('DJ1528+3714-170608.ms', wtsfile='DJ1528+3714-170608.npy') sets up phase centres for the drift scan observation and phase rotates the data to the nearest pointing centre, overwriting the original ms.

4.3.5.4 'FIT SPECTRUM'

This script fits a spectrum to uv-data for a source. For example spec=fit_spectrum(vis='M81-151214.ms', field='1', write_archive=True, nbins=8, archive='/ami/LA/etc/flux_archive',figfile='interleaved_spectrum.png' , showgui=False) will fit the spectrum for the interleaved calibrator source, write the fit to the flux archive and save a plot. Return a dictionary containing the fit with the information necessary for setjy.

4.3.5.5 'FIX SCAN'

This script generates new scan numbers marking field changes. For example fixscan('A1914-150602.ms') generates new scan numbers for each visit to each field during the observation, helpful for controlling calibration operations. Alternatively, fixscan('A1914-150602.ms','A1914-fixed.ms') makes a new MS from the original, with unique scan numbers for each visit to each field (source/calibrator).

4.3.5.6 FLAG ON THE FLY SMOOTHING

This script uses rflag with on-the-fly smoothing in time. For example flagdata_otf_smoothing('A1914-150602.ms') generates new scan numbers for each visit to each field during the observation, helpful for controlling calibration operations. Alternatively, flagdata_otf_smoothing('A1914-150602.ms','A1914fixed.ms') makes a new MS from the original, with unique scan numbers for each visit to each field (source/calibrator).

4.3.5.7 'GENCAL_RAIN'

This script generates a rain gauge correction table which uses the modulated firings of the calibration noise diode to measure changes in the system temperature, which can then be used to correct the data amplitudes. For example, gencal_rain(vis='A1914150602.ms', fitsidifile='A1914-150602.idi', caltable='A1914-150602.rain') generates a frequency-independent rain gauge correction table, reading the system temperature and nominal values from the appropriate file.

4.3.5.8 'MUESLI'

This script subtracts a list of point sources. For examples muesli('A1914-151217.ms',
'A1914-151217.list_add_spec', False, False) subtracts the sources in the text file A1914-151217.list_add_spec from A1914-151217.ms

4.3.5.9 'PB_AMI_DRIFT'

The script performs AMI primary beam correction for a single pointing from a drift scan

Customised AMI primary beam correction for a single pointing map from a drift scan observation, using the fitted AMI parameters for the primary beam sigma as a function of frequency and the sample information provided in a .npy file produced by read_wts_drift.

4.3.5.10 'PB_AMI'

This is an AMI primary beam correction for a single pointing. The primary beam correction for a single pointing AMI map, using the frequency-dependent fit to the primary beam width. If the image is a cube, each frequency will be primary beam corrected individually with the appropriate primary beam size.

4.3.5.11 ‘READ_WTS_DRIFT’

This script outputs a read.wts file output from reduce_dc and add pointing centre information. It read a .wts file output from reduce_dc and add associated pointing centre information from the ms. Output in .npy format.

4.3.5.12 ‘SETJY_AMI’

This script sets I+Q calibrator fluxes for AMI. For example setjy_ami(vis='3C286150602.ms', do_plots=True) sets the model visibility amplitude and phase for 3C286, adjusting for the polarization fraction since AMI measures I+Q.

4.3.5.13 ‘WIDEB_AND_PBCORE_AMI’

Wideband PB-correction on the output of the MS-MFS algorithm where a wide-band Primary-beam correction is as follows:

1. Compute a set of Primary Beams at the specified frequencies
2. Calculate Taylor-coefficient images that represent the PB spectrum
3. Perform a polynomial division to PB-correct the output Taylor-coefficient images from the MS-MFS algorithm (clean(nterms>1))
4. Recompute spectral index (and curvature) using the corrected Taylor-coefficient images.

4.3.6 Step 5: Noise to Weight

This step runs the noiseweight.py which generates a large noise map output by swarp into a weight map which we can use with our source finding software.

4.3.7 Step 6: SWarp

Swarp uses those maps generated from Step 5 to stitch them together into the large raster map. SWarp is a program that resamples and co-adds together FITS images using any arbitrary astrometric projection defined in the WCS standard1. Finally, the default.SWarp file is used as a template to create input files for SWarp for combining the individual pointing centre maps into large raster maps using the raster size and distance between raster centres which run drift.py asks for. If there are existing .SWarp files in the run directory, these will be used rather than creating new ones.

This step uses the noise to weightmap.py and weight to noisemap.py scripts.

4.3.8 Step 7: Weight to Noise

The final step is to run the weightonoise script which will convert the large weight map output by swarp into a noise map which we can use with our source finding software.

4.4 Maps

Drift scans last 30 minutes between calibrations. Discrete pointing centres are defined along each declination strip separated by 10 arcminutes, and the drift scan data points are associated with and phase rotated to their nearest pointing centre; the data are then output as a multisource uv-FITS file. Data from any re-observations of the same pointing centre are stacked together in uv-space. Each of these ~40 second sections of data are used to produce a map known as a pointing. An example of a pointing map generated from the pipeline is shown in Figure 4.2. The map has been corrected for the primary beam, which is why the noise level increases towards the map edges. The primary beam is slightly elliptical, with major axis in the RA direction due to the drift scanning across 10 arcminutes of sky. The map is clipped at the 0.1 point of the primary beam.

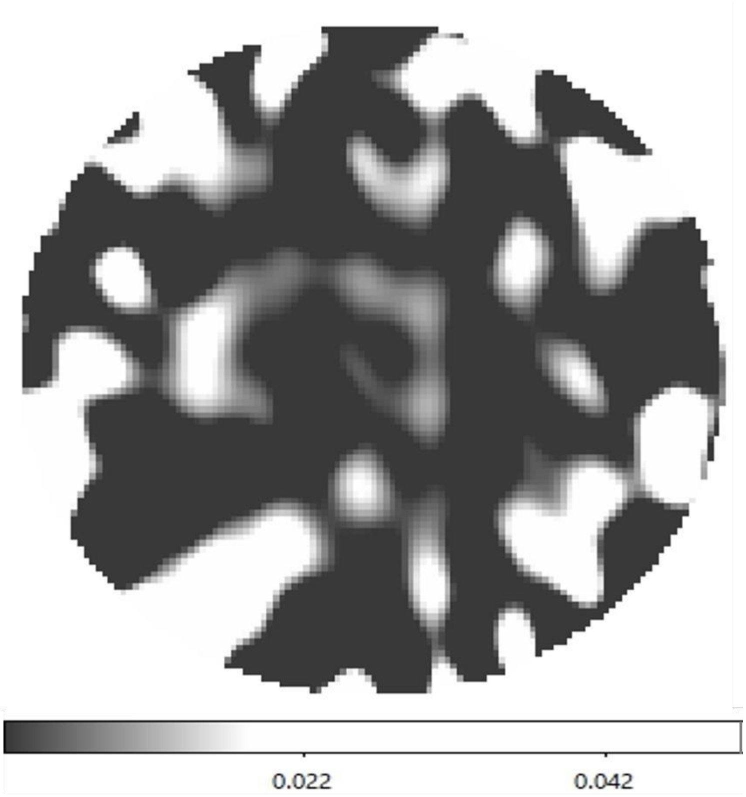

Figure 4.2 A single pointing map from ~40s of data in mJy/beam.

All these pointing maps are then combined to give a long strip map. An example of a strip map is shown in Figure 4.3. These long strip maps are made up of all the field observations within the 30 minutes in between calibrator source observations. The calibrator source is observed then another drift scan is made for 30 minutes, of which every 30 minutes the calibrator source is observed.

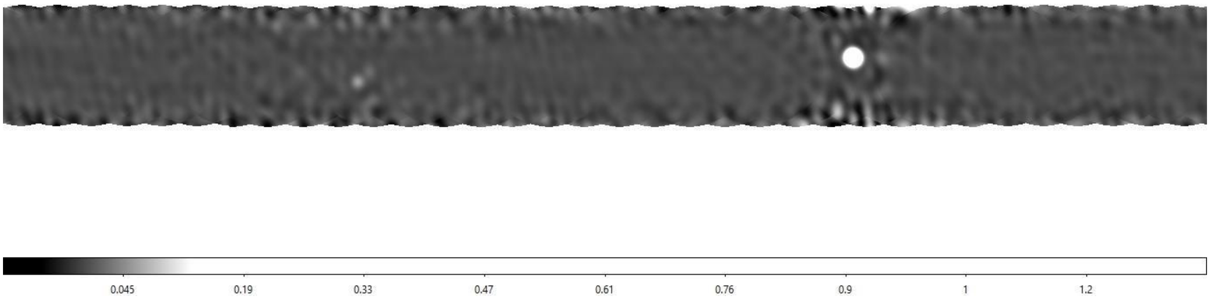

Figure 4.3 A strip map composed of all the pointing maps taken within a 30 minute period between calibrator observations. The height is approx. 20 arcmin and the width is approx. 7.5 degrees

The strip maps from multiple days of observations can then be combined together using SWarp to give a large map covering several square degrees of sky. The map is analysed further to look for sources of interest and also what improvements can be made using better calibration techniques. An example of one of these large maps is shown in Figure 4.4. Three regions have been selected to give an idea about distortion around bright sources. These regions, labelled A, B and C, are shown in closer detail in Figure 4.5 below and the source information from each of the regions A, B and C is contained in Table 4.1.

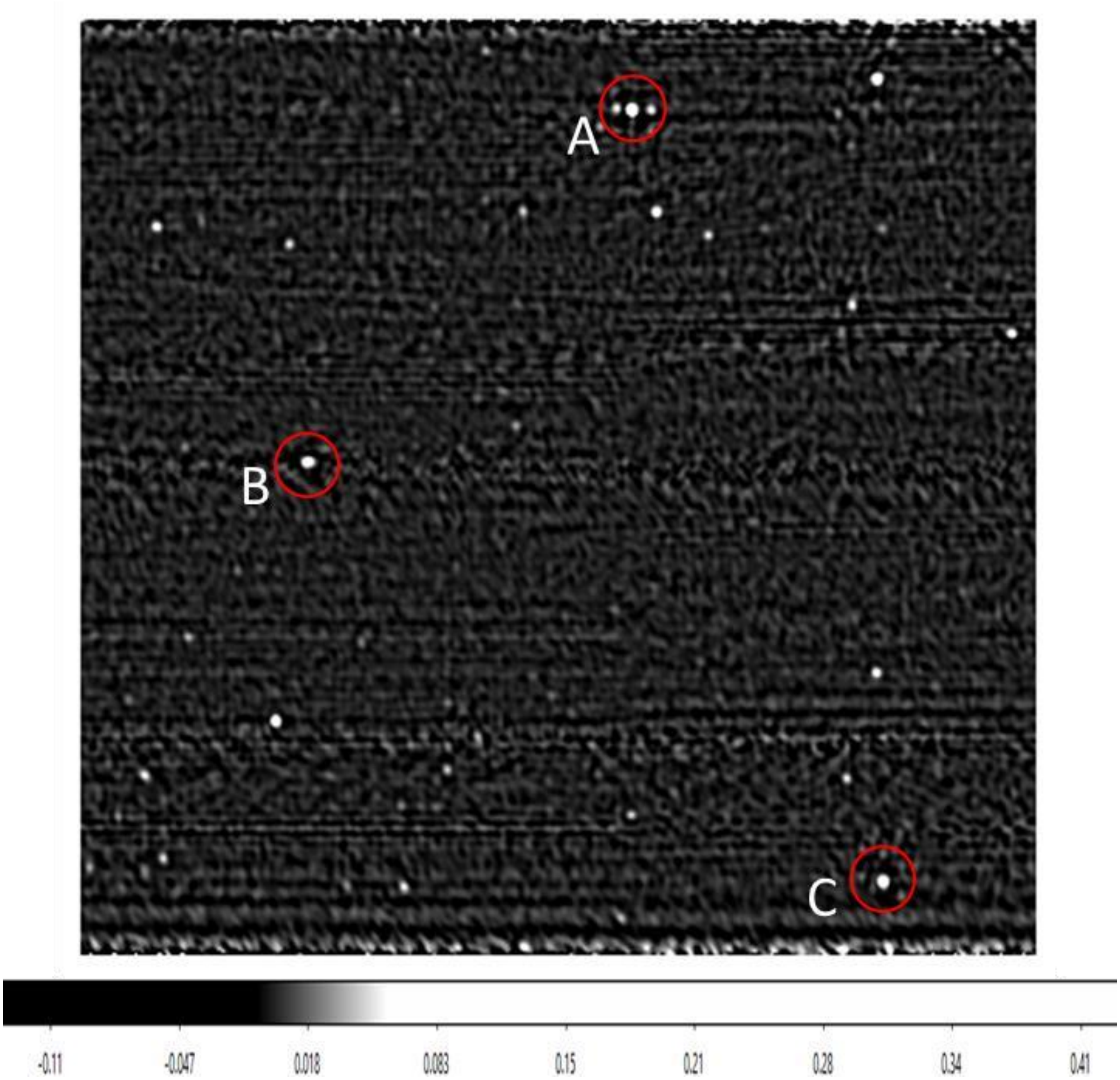

Figure 4.4: map of the sky to show full view of the sky where the individual beamcorrected pointing maps are added together to create a large map approx. 5 x 5 degrees

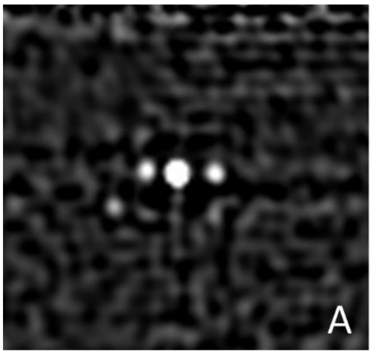

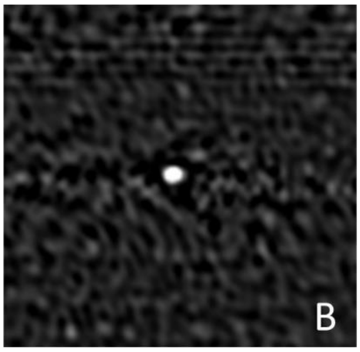

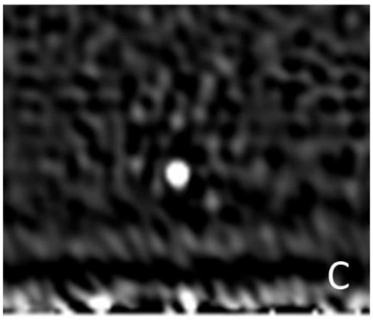

Figure 4.5: up close screen captures of sources labelled A, B and C taken from Figure 4.4. Sizes approx. 1 x 1 degrees (not all quite the same size).

Region	α	δ	Flux / Jy
A	0:29:48.2464	+5:54:56.590	0.447432
B	0:39:19.0818	+3:19:31.080	0.189713
C	O:22:26.8392	+0:15:14.655	0.266052

Table 4.1: information about the sources A, B and C where α is the source inclination, δ is the source declination, and the Flux (S_ν) is given in Janskys in the last table column

4.5 Noise Maps

When the telescope is pointed towards a blank patch of sky, the visibilities will be Gaussian random noise resulting from the non-zero system temperature of the receivers. When imaged, this produces features that are Gaussian, random and centred on zero, giving positive and negative features all throughout the map. The noise level can be estimated by calculating the rms from the pointing maps. Such a noise map is shown in Figure 4.6, though noise maps are also constructed for the strip maps. The noise maps have two main uses. When pointing maps are combined into strip maps and when strip maps are combined into large maps, weighting of each pixel is done according to the inverse variance calculated from the noise map. The noise maps are also used in source-finding, where the local estimate of the noise level is used to define the threshold flux level for identifying sources in order to reduce the chance of spurious detections in regions where the noise is high.

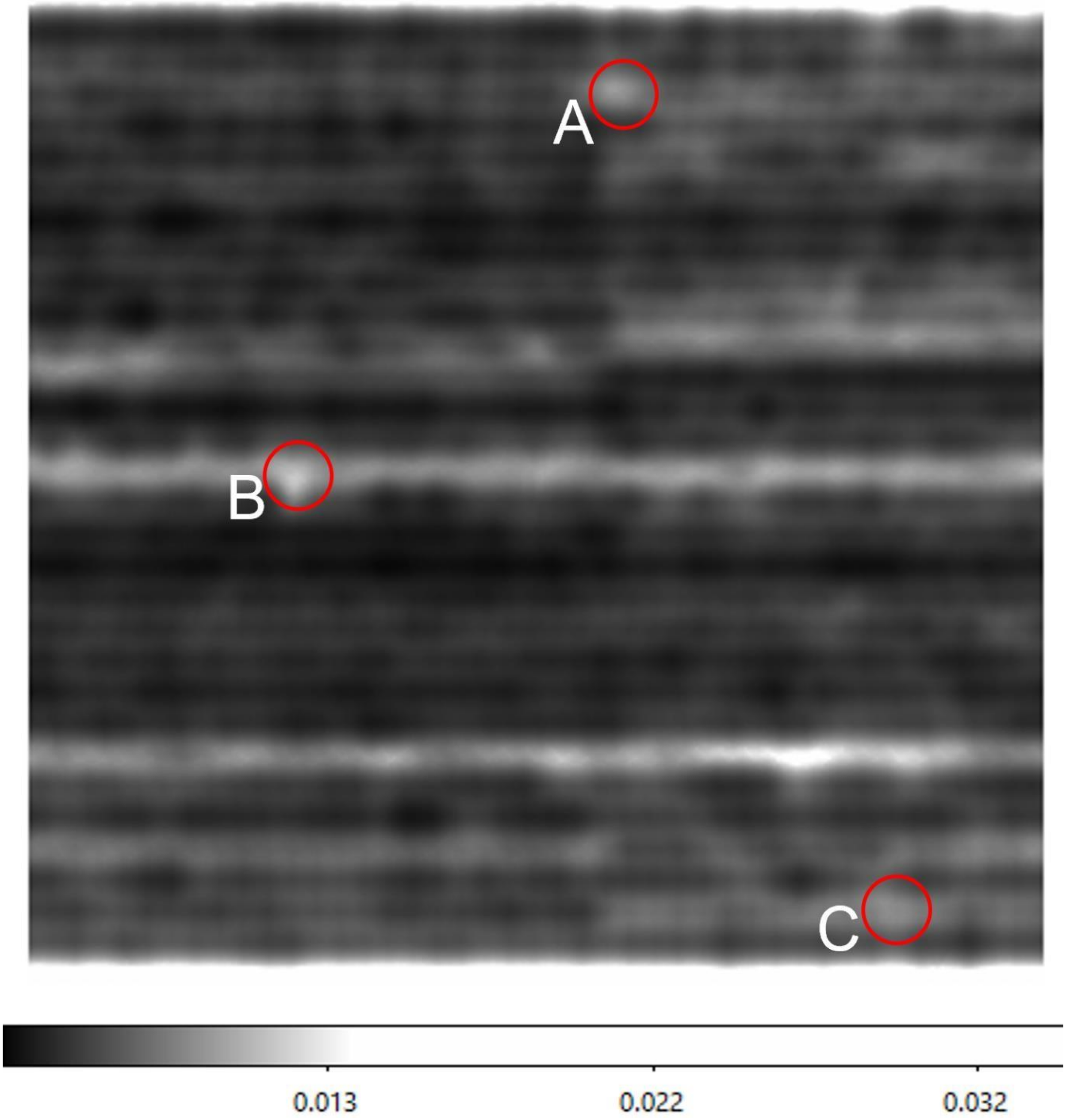

Figure 4.6: Noise map corresponding to the large map shown in Figure 4.4 approx. 5 x 5 degrees

You can see from this noise map there are stripes going across it, which correspond to an observation where the noise level was high. A horizontal strip is all data taken on the same day since drift scans are made at a constant declination. The reason why this observation noise level is high could be either that there a fault with the telescope or that there were poor weather conditions on that day. During scheduling of the observations, a quality assessment needs to be made for the entire strip about whether the weather was adequate or if the strip needs to be re-observed.

In the regions around a bright source the noise level might appear higher. This is because, due to calibration errors, some of the flux of the source effectively leaks into the surroundings, increasing the local variance. This arises because the visibilities that are measured have gain errors (both amplitude and phase) with the result that a bright source does not map perfectly to a psf (point spread function) during the imaging step, with the result that (after CLEANing) the region round the source has artefacts that might be misinterpreted as real sources.

The aim of this thesis is to try to improve calibration to minimise these distortion effects so that the artefacts are not generated and the noise level around the sources is reduced. The importance of this can be illustrated from image A in Figure 4.5, which contains a main source in the centre and two additional sources to either side. It is likely that these three features represent emission from three separate components from a single extended astrophysical object. However, there are clear artefacts to the south of these three components, so it would be difficult to be confident about concluding much about the shape and structure of this extended source. These artefacts are caused by mis-calibration of the bright sources, so improvement of the calibration would ideally lead to an image having none of these artefacts so that all the bright features on the map can be believed.

In addition to this, the artefacts caused by poor calibration will increase the apparent noise level round the bright source with the result that real sources in the vicinity will not stand out above this increased noise and not be identified. Improved calibration techniques will reduce the noise level and therefore the threshold flux for identifying sources, leading to additional sources being discovered and added to the catalogue.

4.6 Duplicate Sources

For any two strip maps, the drift scan observations may produce some overlap on the edges of each map as shown in Fig 4.7. These small discrepancies at the edges of the maps are because Map 1 may look at a particular calibrator source, Calibrator 1, yet Map 2 uses a different calibrator source Calibrator 2. This could produce a situation in which the same source will be found in both of those 2 maps appearing right on the edge of one map and on the left of another map. These are 2 independent measurements of the same source.

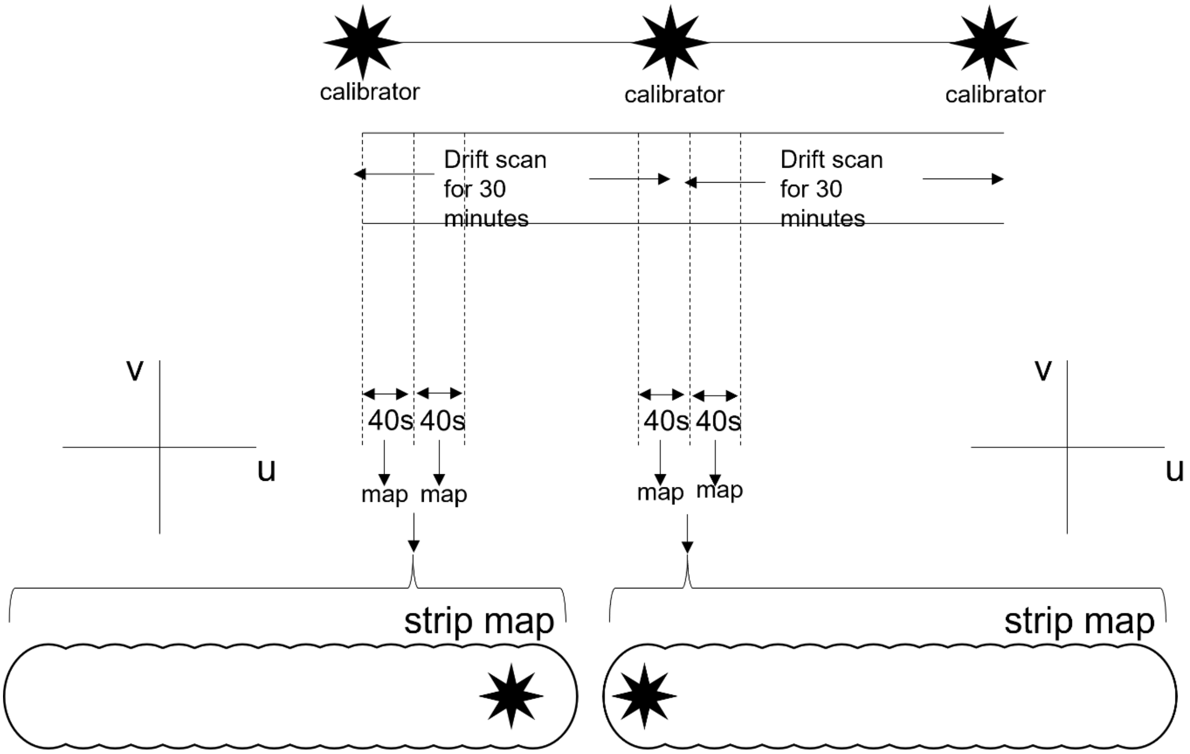

Figure 4.7: Diagram of the process of drift scanning

The phase of a calibrator can be measured and assumed to go linearly between two points. From this a correction phase can be calculated by how the standard interleaved calibration works. This results in a different phase calibration to each set of data and so the phase calibration is different.

Furthermore, for each drift scan observation, the telescope is stationary and so the azimuth and elevation of the sky remains the same and the sky ‘drifts’ by. This means that for the next drift scan observation, the azimuth and elevation will be different. This is important because the azimuth and elevation depend on what the uv coverage is and so the uv coverages for these two blocks are going to be different as well which also means the point spread function will be different and all other sorts of things. In summary, a different phase calibration has been applied to each dataset and a different uv coverage has been generated.

It is ideal that the 2 small maps would show the source being near identical. However, it will not be identical as different data is being used. Different chunks of different 40 seconds worth of data results in different calibration and different intrinsic uvcoverages. This then gives an indication of how repeatable our observations are. An example of a duplicate source is the source 1:15:40.0694, +3:56:02.342 which can be seen to the far right of map J0129+0308 and the same source appears in map J0102+0308 to the far left of the map.

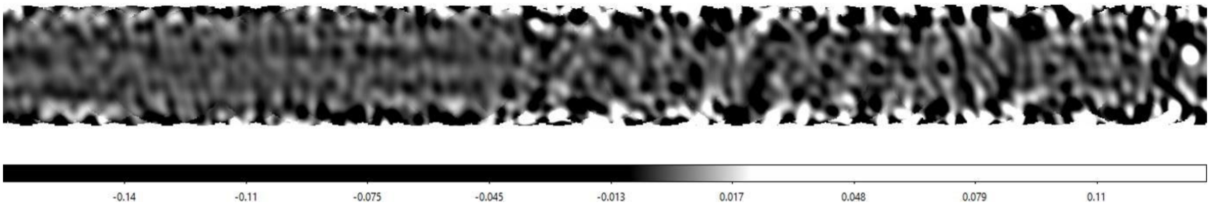

Figure 4.8: Strip map J0129+0308. The height is approx. 20 arcmin and the width is approx. 7.5 degrees.

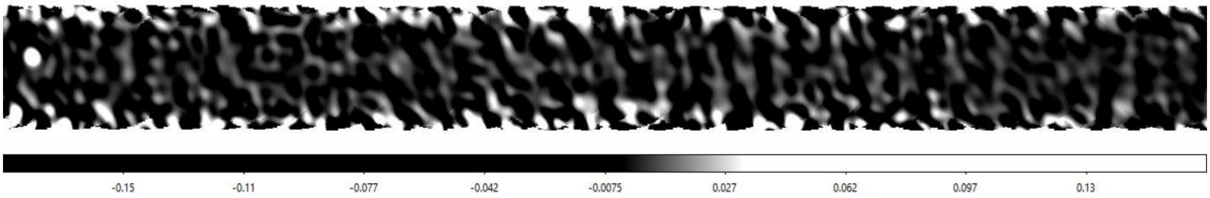

Figure 4.9: Strip map J0102+0308. The height is approx. 20 arcmin and the width is approx. 7.5 degrees.

The centre of each region taken from the map is 18.9, 3.94 for both sources, with corresponding co-ordinates of the source as 1:15:40.0694, +3:56:02.342 where 1 pixel is equal to 15 arcsec. Table 4.2 shows the results from the information taken from each region giving very similar results showing that even though the same 40 seconds of data has been reduced using different techniques it shows very similar results whereby the rms can be seen to be almost identical as the maximum brightness of the centre of each source.

map	min	max	rms
J0102+0308.fits	-0.002	0.12	0.055
J0129+0308.fits	-0.001	0.12	0.055

Table 4.2: Information about the source contained within both strips

5 Self-Calibration

As discussed in Section 2.8, at 15 GHz the troposphere introduces significant distortions in the wavefront of the radio signal which results in both amplitude and phase distortions to the visibilities measured by correlating the signals between two antennas. The standard procedure to attempt to remove these errors is to produce a calibration based on periodic observations of a nearby, bright point-source, which are interleaved with observations of the field being observed. This procedure makes the assumption that the distortions introduced by the troposphere towards the calibrator are identical to those towards the field, and that any time varying changes can be well modelled with an interpolation between the calibrator measurements (Kasuga et al., 1986). In practice, interleaved calibration typically works adequately well, though it is not perfect. However, if the field contains a bright source, the imperfections in the interleaved calibrations arising from errors in the assumptions can result in flux from the source being mapped to the wrong position, which results in the appearance of “artefacts”, which are bright features in the map that can be misinterpreted as being real radio sources. A method for dealing with these errors is self-calibration.

5.1 Principle of Self-Calibration

Self-calibration uses a source within the field being observed itself to better calibrate the antenna-based complex gains, removing amplitude and phase corruptions as a function of time. A model of the source is produced, and gain calibrations are solved for the best match of data to the model. The model of the source is generated initially through imaging the source through quick-look data in the case of this research. This process is illustrated in Figure 5.1 In practice it is often the case that self-calibration is run separately for phase and amplitude in separate iterations, with most often a phase only self-calibration iteration being followed by an amplitude or combined amplitude and phase iteration.

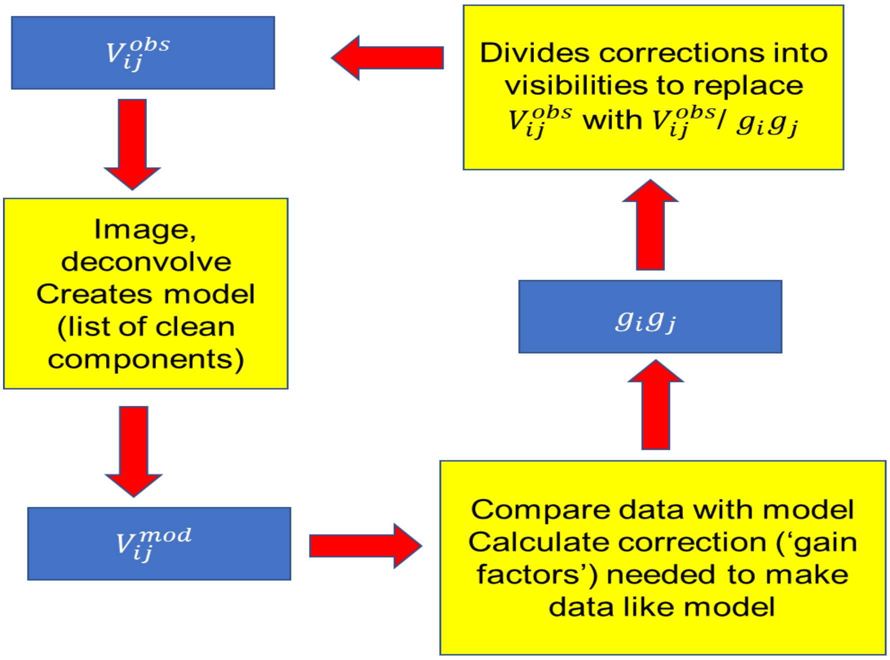

Figure 5.1 The self-calibration loop. The visibility data is mapped and from this a model for the brightness distribution in the field is produced. This model is used to simulate expected visibilities and these are then compared with the data themselves. From this comparison, antenna based gain corrections are calculated which would minimise the difference between the true visibilities and the model predicted values. These gains calibrations are then applied to the visibilities. It is then possible to iteratively repeat the whole calibration loop in order to identify and remove lower level antenna based gain errors.

5.2 The Self-Calibration Model

The first step in self-calibration is to generate theoretical visibilities from a model of the sky. A simulated visibility is calculated from antenna positions and source positions using the measurement equation

$$V_{ij} = \int I(s)\, e^{-2\pi i \nu \frac{\vec{b}\cdot\hat{s}}{c}} \qquad (5.1)$$

where $I(\hat{s})$ is the sky brightness distribution, $\vec{b}$ is the baseline vector which is equal to $\vec{a}_i - \vec{a}_j$ baseline vector and $\hat{s}$ is the source direction and c is the speed of light in a vacuum. It is assumed that the antenna positions, a_i, are well known through a combination of surveying and observations of bright astronomical sources.

In order for self-calibration to work, at least one bright source is needed for the model. If this technique is applied to a faint source, then when the position is measured, there will be a significant error on the estimate, which is roughly the size of the synthesised beam divided by the signal to noise ratio (SNR) of the source. If the position used in the self-calibration model is badly wrong, as may well be the case for a faint source measured with low SNR, then the self-calibration may well fail and make the image worse. In summary, for the self-calibration model to work, a good estimate of the source position is needed and to get a good position a bright source is needed.

5.3 Phase Self-Calibration

Once the model visibility has been generated, phase self cal attempts to find antenna based phase correction terms, θ_i, which minimise the difference in phase of the measured visibilities, $\phi(M_{ij})$, and the phase of the modelled visibilities, $\phi(V_{ij})$. Each baseline will yield an equation like

$$\Delta\phi_{ij} = \phi(M_{ij}) - \phi(V_{ij}) = \theta_i - \theta_j . \qquad (5.2)$$

Taking AMI-SA as an example because it has 10 antennas, there are 45 baselines and thus 45 simultaneous equations to be solved. Since interferometry measures phase differences between antenna pairs, there is no absolute definition of zero phase, and so one antenna is designated as the reference antenna and there are only 9 antenna phase correction terms to be fitted. Since there are 45 simultaneous equations and only 9 unknowns, this is an over constrained problem and a solver can find best fit phase corrections. These calibrations can be applied to the measured visibilities, which can be remapped and used to define an updated model to allow further iterations of phase self-calibration, or amplitude calibration.

5.4 Amplitude Self-Calibration

Amplitude self-calibration is similar to phase self-calibration except that instead of taking the difference of parameters, the products of antenna based gains are taken. This then means that overall, there is a sensitivity to an absolute scale now.

Differences are not taken so the actual value of these parameters can be solved for and for AMI there are 10 unknowns. Amplitude self-calibration therefore attempts to find antenna based amplitude correction terms, g_i, which minimise the difference of the ratio between the measured visibilities, $A(M_{ij})$, and the amplitude of the modelled visibilities, $A(V_{ij})$. Each baseline will yield an equation like

$$A(V_{ij}) = g_i g_j A(M_{ij})\,. \tag{5.3}$$

This correction will be a multiplicative factor for adjusting the amplitudes so that all the data agree on the amplitude for this source. Again, since there are 45 simultaneous equations and only 10 unknowns, this is an over constrained problem and a solver can find best fit amplitude corrections. These calibrations can be applied to the measured visibilities, which can be remapped and used to define an updated model to allow further iterations of self-calibration if necessary.

5.5 Weighted Self-Calibration

The different antennas in the AMI-SA all have different T_{sys} performance. This is for multiple reasons, though the dominant one is the variation in the first cryogenic lownoise amplifier in the receiver due to manufacturing tolerances. As a result, each baseline will have a different noise level on its visibilities, which can be estimated though measuring the rms towards a blank patch of sky (in practice, any patch of sky without a very bright source in the field). Since the equations for each baseline given in 5.2 and 5.3 form an over-constrained set for determining the antenna gains, a best fit has to be sought, and the default algorithm treats all of the input data with equal weight. However, given that we have estimates of the noise levels associated with each baseline we can instead perform the fit which gives additional weight to the data with the best SNR. This is known as weighted self-calibration.

5.6 Time Interval and Frequency Sub-Band Self-Calibration

The phase and amplitude self-calibration algorithm as described above fits for a single complex gain within all the time-stream data of a pointing's observation and for all the frequencies between 13 and 18 GHz. This assumes, in the case of phase, that the phase from the atmosphere doesn't change during the time of the pointing's observation, which for the AMI drift scans is approximately 40 seconds. Similarly, it is assumed that the phase correction for all frequencies within the band are the same. Both of these assumptions are likely to be approximately true, but it is possible to relax these by specifying a time interval and / or sub-bands during self-calibration.

Using a time interval, the data is broken into different time sections and selfcalibration is applied independently to each. This can reveal information about whether or not the atmosphere changes throughout these different time chunks. The choice of whether to apply a time interval is non-trivial and depends upon the observation and the brightness of the self-calibration source. A consistent atmosphere would mean breaking up the data into independent chunks, which will reduce the overall signal-to-noise available for the self-calibration and therefore will make the fit a lot worse. In this case, it might not be worth accounting for time interval calibration. A similar argument applies to breaking the data into separate subbands. For example, if we were to run self-calibration over 1GHz sub-bands (from the 5 GHz total bandwidth) and apply a 10 second time interval (from the 40s total time stream data), will result in only $\frac{1}{20}$th of the total amount of data being available for the fit. This would result in the noise of each baseline's measured visibility increasing by a factor of approximately $\sqrt{20}$ and so the fit is worse by this amount. However, if the source is really bright, then the increase of the noise by an amount of $\sqrt{20}$ possibly is insignificant compared to the source flux. This again points to why a bright source is preferred in order to perform self cal. In practice, an experimental approach is adopted to determine the optimum time interval and sub-band definitions. Results will therefore show whether or not the atmosphere is changing or is stable by showing whether applying this technique to the data improves the final map or not.

5.7 Self-calibration on AMI drift scan data

Self-calibration is a standard technique to apply in radio interferometry, but particular problems do exist for its application to the AMI drift scan data. Firstly, during the initial interleaved calibration step, it is assumed that the calibrator source is close to the area of sky that is being observed. Scanning the first section of data might correspond to the first calibrator source residing close to the data but as the observation progresses the distance to the calibrator will become large. Different calibrator sources are used during a long observation that are now closer to the patch of sky being observed, but this means that the interpolation between the interleaved measurements spans a large displacement across the sky with potentially significantly different troposphere. This could result in larger calibration errors than for traditional tracking observations, with the result that the maps used to generate the selfcalibration models will be relatively poor quality resulting in a poor model being used at the fitting stage. Secondly, the observations of the bright sources used during selfcalibration are necessarily short and so the uv-coverage is not improved by Earth rotation meaning that the dirty beam will have significant sidelobes. Again, this will impact the accuracy of the model being used for self-calibration. Thirdly, given that the bright source is drifting through the telescope's beam during the observation, its observed flux will be modulated by the primary beam response and this modulation will change dramatically even during the 40s of data going into a single pointing observation. The modulation can be calculated based upon a model of the primary beam, but then additional errors due to telescope pointing offsets and inaccuracies in the primary beam model itself will potentially impact the fit. Since the purpose of selfcalibration is to remove errors resulting from factors beyond those that are theoretically predictable, simulating the impact of these effects is very difficult and so it is best to study the data themselves.

6 Optimising self-calibration for AMI drift scans

6.1 AMI Drift Scanning Procedure

The data reduction pipeline described in Chapter 4 is run on the visibility data, which implements procedures such as flagging, calibrating etc. then a small amount of time ordered data that was looking close to or at a particular RA and Dec. The full drift scan run is split to divide the visibility data into separate parts, each associated with an individual pointing centre. This data is mapped to give an individual pointing map $x(i, j)$ where i and j represent the pixel coordinates in RA and Dec. The noise level across this map can be assumed to be approximately constant. This can be estimated by finding the rms in the individual pointing map far from any bright sources. The estimated noise map $s(i, j)$ is a uniform level as found above. These individual maps need to be primary beam corrected, and since this is a drift scan observation the telescope is looking along a variety of RAs even within an individual pointing map so the primary beam is very slightly elliptical which can be represented as $p(i, j)$.

The primary beam corrected map is retrieved by dividing through by the primary beam. This produces a primary beam corrected map $X(i, j)$. This primary beam corrected map is hence

$$X(i, j) = \frac{x(i, j)}{p(i, j)}. \tag{6.1}$$

After the correction of the primary beam is performed then sources in the map will now appear with their intrinsic flux. However, the original map had uniform noise everywhere and so after we've divided through by the primary beam means that we get all the sources being the correct flux, but it also has magnified up the noise. This change in the noise map due to the primary beam correction can be represented as $S(i,j)$ where

$$S(i,j) = \frac{s(i,j)}{p(i,j)} \tag{6.2}$$

The maps are cut off and 'blank' in regions where $p(i,j) < 0.1$.

An optimal weighting map corresponding to the primary beam corrected map can also be defined as $W(i,j)$ where

$$W(i,j) = \frac{1}{S(i,j)^2}$$

This above procedure can now be repeated for all of the visibility data giving a large number, N, of individual maps. Let's have $a = 1 \ldots N$. The primary beam corrected versions are X_a, S_a and W_a which are all centred on a different RA and Dec. These N maps are all combined together onto a single map called $\xi(I,J)$ which has a corresponding weight map $\omega(I,J)$.

We need to be able to displace each of the individual maps (i,j) onto the new grid (I,J). For each pixel (I,J) which of the individual maps have mapped this pixel needs to be found. A weighted combined map can be produced

$$\xi(I,J) = \frac{\{\Sigma\, W(I,J) X(I,J)\}}{\{\Sigma W(I,J)\}} \tag{6.3}$$

$$(I,J) = \frac{1}{\sqrt{\left(\omega(I,J)\right)}}$$

and

$$\omega(I,J) = \Sigma W(I,J) \qquad (6.4)$$

An estimated combined noise map $\sigma(I,J)$ can be produced as

$$\sigma \qquad (6.5)$$

6.2 Initial Self-Calibration Tests on J0116-0010

This standard procedure was run for a data set containing a ~100mJy source towards J0116-0010. The source was then remapped after applying a standard self-calibration strategy both with and without calibration weighting applied in order to evaluate them. Maps are shown in Figure 6.1 and statistics in Table 6.1.

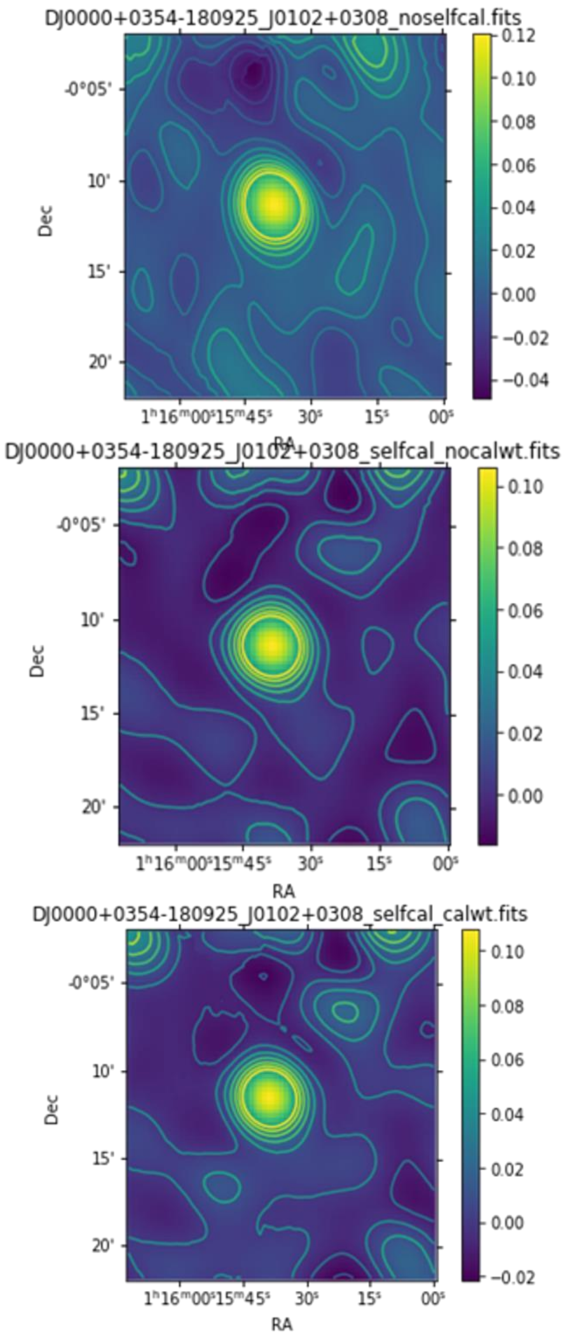

Figure 6.1: Maps of the bright source at J0116-0010. Top – no self-calibration. Middle – standard phase selfcalibration. Bottom – phase self-calibration with calibration weights applied. Contours are in 10mJy steps.

method	min	max	rms
no selfcal	-0.0203	0.1202	0.0442
calwt=false	-0.0147	0.1057	0.0275
calwt=true	-0.0149	0.1076	0.0282

Table 6.1 Results of self-calibration tests towards J0116-0010

Looking at Figure 6.1 and comparing the no selfcal with selfcal we can see it has visibly made a difference to the image quality. 20mJy features are visible to the southwest of the source which are artefacts produced by calibration error. Applying selfcal to the same data produces a better map with fewer artefacts. The statistics in Table 6.1 confirm the improvement since the level of the most negative feature is reduced (a useful diagnostic since the sky should be positive definite) and since the rms is also reduced. Hence, the selfcal procedure is improving the data quality and removing phase errors present in the visibilities. Either applying or not applying calibration weights makes little difference to the image quality or the map statistics.

Further experiments were then performed towards a brighter, 1.3 Jy source, since the effects of self-calibration should be more significant, and it would therefore be possible to investigate optimising the self-calibration strategy. While it was clear that self-calibration was still improving image quality, the results were disappointing and upon investigation, a flaw in the experimental procedure was discovered. Figures 6.2 and 6.3 show the strip map and noise map towards the 1.3 Jy source. It is clear that the noise level is increased round the bright source, as expected due to calibration errors. However, as a result, the pointing map that contains the bright source has a higher noise level than the adjacent pointing maps and as a result it is significantly down-weighted compared to these when SWarp combines the pointing maps together. The impact of this is that the strip maps in the vicinity of the source are dominated not by the pointing map in which self-calibration will be making the most improvement, but by the surrounding maps where self-calibration both has less scope to make improvements and limitations from poor knowledge of the primary beam will result in a poor model for self-calibration. Therefore, the process of combining pointing maps with SWarp and assessing results in the strip maps is masking the effects of self-calibration. Because of this, for further investigations, individual pointing maps were looked at for analysis.

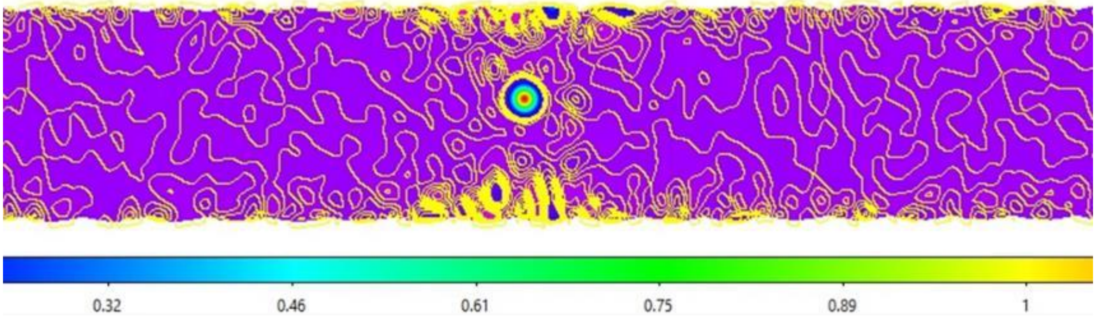

Figure 6.2 Strip map towards a bright 1.3 Jy source.

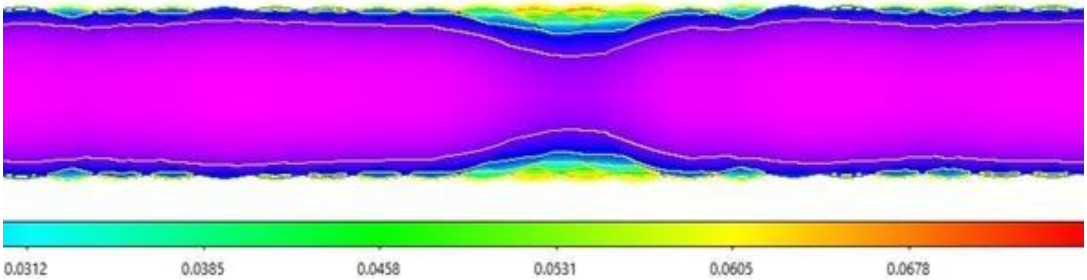

Figure 6.3 Noise map corresponding to Figure 6.3

6.3 Self-Calibration Tests on Pointing maps

6.3.1 Noise Level Determination

In order to determine in an absolute sense how well self-calibration was performing, a pointing map made from the same day's drift scan as the one containing the bright source but for a field with no sources present was analysed and is shown below in Figure 6.4. This map of blank sky can therefore give us a good estimate of the thermal noise that should be present in a pointing map by calculating the noise in the centre of the map. It was important to only use the centre of the map because the primary beam correction will magnify up the noise level towards the map edges and give a biased estimate. The noise level was found to be 7 mJy and further statistics are given in Table 6.2.

	min	max	rms
background	-0.0171	0.0168	0.0073

Table 6.2: Statistics in a blank sky pointing map

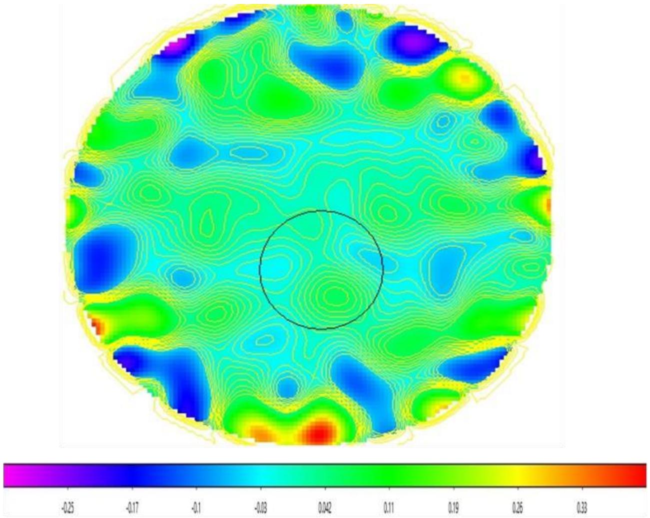

Figure 6.4: Pointing map of a black patch of sky

6.3.2 Different Self-Calibration Strategies Explored

The drift scan including the bright 1.38 Jy source J0122+0422 was reduced with a modified version of the AMI pipeline that retained the individual pointing maps for analysis. Six different calibration scenarios were explored. These were:

1) Standard interleaved calibration. This was the “control” test with only standard interleaved calibration and no self-calibration applied.

2) Phase self-calibration. Self-calibration only for phase corrections with infinite solution interval, which effectively smooths over all data samples within a given pointing's visibility set and similarly smoothing over all channels.

3) Interleaved-bandpass phase self-calibration. As 2) but these correspond to 13 – 15.5 GHz and 15.5 – 18 GHz and after the down-conversion through a heterodyne mixer, the two spectral windows follow different receiver paths through a second down-conversion stage and through different digitisers and digital processing (Fried, D. L, 1966). Due to these differences, it might not be surprising if self-calibration found different gain solutions for the two spectral windows, so this set up gave selfcalibration the flexibility to search for such a solution at the expense of a degradation in SNR of $\sqrt{2}$ due to the reduced bandwidth available for each individual solution.

4) Phase and amplitude self-calibration. Self-calibration attempts to find both amplitude and phase based antenna gain correction terms.

5) Interleaved-bandpass, phase and amplitude self-calibration. As 4) but allowing for different solutions to the two different AMI spectral windows.

6) Phase self-calibration, followed by amplitude and phase self-calibration. As 2) but then followed by a second iteration of self-calibration in which both amplitude and phase corrections are fitted for simultaneously.

6.3.3 Results and Discussion

The following results obtained from the self-calibration strategies discussed above are shown in Figure 6.5 and Table 6.3.

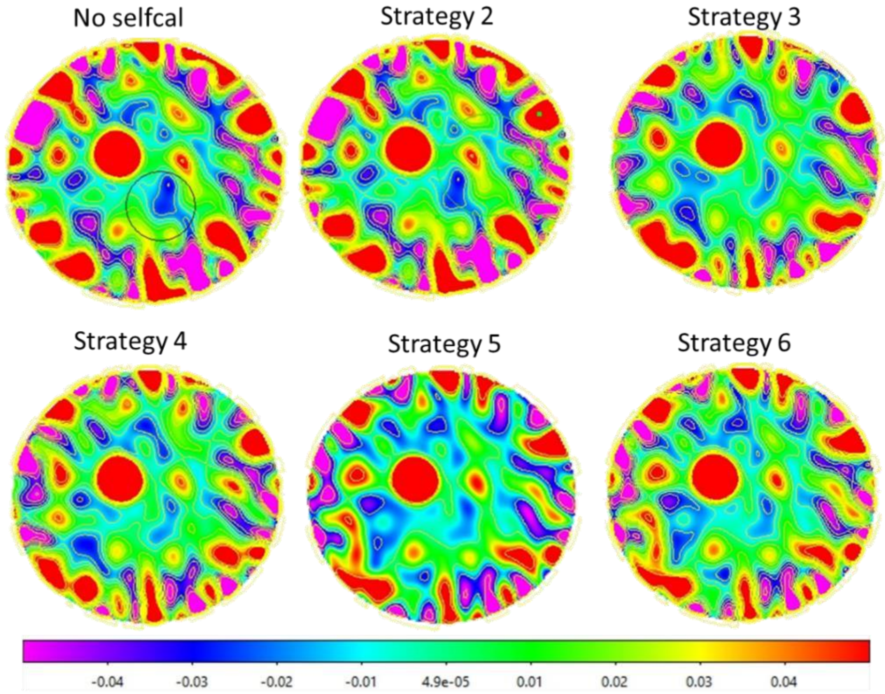

Figure 6.5. Comparison of the 6 different calibration techniques applied. Source strength is 1.38 Jy and the position is at α 1:21:57.0447, δ +4:22:22.485.

The black circle on the "no selfcal" map is the region used to calculate the statistics which are presented in Table 1. The coordinates of the centre of the region used for background noise analysis are 1:21:33.0000, +4:15:05.000 and the size was 0.08 degrees where 1 pixel = 15 arcsec. The region is small but needs to exclude the source itself, and the imaging artefacts occur close to the source. As these are pointing maps not strip maps, the primary beam correction starts to dominate the rms statistics the further away from the pointing centre of the map. Taking these considerations into account resulted in the constrained area indicated on the maps, although this does result in the error on the rms being quite large.

An initial analysis of the results is done by eye to show whether or not and which calibration techniques are worth implementing. Initially, it can be seen quite obviously that even a basic self-calibration strategy makes a difference to the image going from Strategy 1 to Strategy 2.

The rms is decreased by a factor of 1.5, which shows significant improvement. We then see that all the self-calibration strategies show similar results in rms noise, but none of them reach the thermal noise of 7 mJy.

Selfcal Strategy	min	max	Rms
No selfcal	-0.0317	0.0310	0.0172
2	-0.0245	0.0359	0.0115
3	-0.0242	0.0282	0.0119
4	-0.0252	0.0365	0.0128
5	-0.0197	0.0337	0.0121
6	-0.0261	0.0317	0.0116

Table 6.3: Statistics for each of the maps within the analysis circle.

It was concluded that some other instrumental factor is limiting the dynamic range of the telescope. Motivated by that, various different implementations were tried by self-calibration by considering different versions of selfcal such as applying calibration weighting, applying reduced calibration intervals and separating different sub bands etc. None of these self-calibration techniques made a significant difference to the output maps and none actually fix or improve the selfcal over and above the amount needed for sufficiency. From this we conclude that selfcal is the right thing to do but there is no clear indication from the maps of an optimal selfcal strategy. In order to improve things and hopefully get further towards the thermal noise will require further investigation beyond scope of project.

7 Conclusion & Further Work

The key finding of this work is that introducing a self-calibration step into the AMI data reduction pipeline does improve the image quality for fields with sources brighter than 100 mJy. It was also discovered that assessing the impact of different self-calibration strategies was complicated by the process of performing a weighted combination of the individual pointing maps into strip maps. The weighting procedure had the impact of disguising any improvements in the map centred on the source resulting from running self-calibration. It was concluded that assessments of selfcalibration must be performed on the individual pointing maps.

For sources of around 1 Jy it was again found that applying phase self-calibration significantly improved the image quality. However, the noise level in the map was still significantly higher than the thermal noise, indicating that for such bright source residual calibration errors were causing some of the source flux to be mapped incorrectly. More sophisticated self-calibration strategies were explored, including use of amplitude calibration, use of baseline weights during the fitting procedure and fitting separately for the two AMI sub-bands, but none of these approaches gave significantly better results than the simple phase self-cal. Some other instrumental factor was concluded to be limiting the dynamic range of the telescope and further investigation of this is needed to reveal whether or not this is the case.

After the research for this thesis was concluded, it was subsequently discovered that an error in the absolute time stamps implemented in the "quick look" pipeline was resulting in a positional offset in the maps used to define the model used in the selfcalibration (Joel Miller, private communication). This would necessarily limit the degree to which self-calibration could correct for errors introduced by the troposphere.

The AMI drift scan survey has now completed observations of approximately half of the 20,000 square degrees of the northern hemisphere. As a result of this work, a self-calibration step will be included in the standard data reduction pipeline when the full data set is analysed. The completed 11C survey from these observations will provide a valuable legacy survey to the astronomical community since it will be the deepest survey of a substantial fraction of the sky at frequencies higher than 5 GHz.

References

Airy G., Wave Theory of Light: This Pattern Consists of Concentric Light Regions Alternating with Dark Ones., 1835

Andrew A. et al., Interferometric Imaging Directly with Closure Phases and Closure Amplitudes, Harvard-Smithsonian Center for Astrophysics, USA, 2018

Armstrong J. & Sramek R., Observations of Tropospheric Phase Scintillations at 5 GHz on Vertical Paths, Radio Sci., 17, 1982, p. 1579–1586

Asaki Y. et al., ALMA Fast Switching Phase Calibration on Long Baselines, in Ground-Based and Airborne Telescopes, Proc. SPIE, 2014

Asaki Y. et al., Phase Compensation Experiments with the Paired Antennas Method, Radio Sci., 31, 1996, p. 1615–1625

Bajkova A. & Pushkarev A., Multifrequency Synthesis Algorithm Based on the Generalized Maximum Entropy Method: Application to 0954+1658, Central (Pulkovo) Astronomical Observatory of RAS, Crimean Astrophysical Observatory, 2011

Baldwin J. et al., The 6C Survey of Radio Sources - I. Declination zone $\delta>+80_{o}$, Monthly Notices of the Royal Astronomical Society, Volume 217, Issue 4, 1985, p. 717–730

Barrett A. & Chung V., A Method for the Determination of High-Altitude Water-Vapor Abundance from Ground-Based Microwave Observations, J. Geophys. Res., 67, 1962, p. 4259–4266

Battat J. et al., Atmospheric Phase Correction Using Total Power Radiometry at the

Submillimeter Array, Astrophys. J. Lett., 616, 2004, L. 71–74

Becker R., White R. & Helfand D., The FIRST Survey: Faint Images of the Radio Sky at

Twenty Centimeters, Astrophys. J. 450, 1995, p. 559 -577

Bhatnager S. & Cornwell T., "Adaptive Scale Sensitive Deconvolution of

Interferometric Images I. Adaptive Scale Pixel (ASP) Decomposition", Astronomy and

Astrophysics, vol. 426, 2004, p. 747–754

Bieging J. et al., Interferometer Measurements of Atmospheric Phase Noise at 86 GHz,

Radio Sci., 19, 1984, p. 1505–1509

Born M. & Wolf E., Principles of Optics, Sixth (Corrected) Edition, Pergamon Press, 1980

Briggs D., Schwab F. & Sramek R., Synthesis Imaging in Radio Astronomy II, ASP Conference Series, Volume 180, 1999, p. 127

Christiansen W. & Hogbom J., Radiotelescopes, Second Edition, Cambridge University Press, 1985

Clark B. et al., Coherence in Radio Astronomy, Synthesis Imaging in Radio Astronomy, ASP Conference Series, Vol. 180, 1999

Clark B., An Efficient Implementation of the Algorithm 'CLEAN', Astron. Astrophys. 89,

1980, p. 377-378

Cohen et al., The VLA Low-Frequency Sky Survey, 2007

Condon J. et al., The NRAO VLA Sky Survey., Astron. J. 115, 1998, p. 115, 1693-1716

Corby J. et al., An ATCA survey of Sagittarius B2 at 7 mm: Chemical Complexity Meets

Broad-Band Interferometry, Monthly Notices of the Royal Astronomical Society,

Volume 452, Issue 4, 2015, p. 3969–3993

Cornwell T. & Braun R., Deconvolution., Ch. 8 in Synthesis Imaging in

Radio Astronomy: Third NRAO Summer School, 1988

Cornwell T. & Fomalont E., Synthesis Imaging in Radio Astronomy II.

Astron. Soc. Pac., San Francisco, Vol. 180, 1999, p. 151-187

Cornwell T., Image Restoration (and the CLEAN Technique)., Lecture 9.

NRAO VLA Workshop on Synthesis Mapping, 1982, p. 113

Frater R. & Docherty I., On the Reduction of Three-Dimensional Interferometer

Measurements, Astrononomy and Astrophysics, vol. 84, 1980, p. 75–77

Freeman R., Radio System Design for Telecommunications (1–100 GHz), Wiley, New

York, 1987

Fried D., Optical Heterodyne Detection of an Atmospherically Distorted Signal Wave

Front, Proc. IEEE, 55, 1967, p. 57–67

Fried D., Optical Resolution Through a Randomly Inhomogeneous Medium for Very

Long and Very Short Exposures, J. Opt. Soc. Am., 56, 1966, p. 1372–1379

Fried D., Statistics of a Geometric Representation of Wavefront Distortion, J. Opt. Soc.

Am., 55, 1965, p. 1427–1435

Graham A. et al., History of Astronomy in Australia: Big-Impact Astronomy from World

War II until the Lunar Landing, Galaxies, 2021, p. 1945–1969

Grainge, K. & Scaife, A., Radio Astronomy, The University of Manchester, 2019

Hales S. et al., A Final Non-Redundant Catalogue for the 7C 151-MHz Survey, Monthly

Notices of the Royal Astronomical Society, Volume 382, Issue 4, 2007, p. 1639–1642

Hales S. et al., A Revised Machine-Readable Source List for the Rees 38-MHz Survey,

Mon. Not. R. Astron. Soc., 1995, p. 274 – 447

Hickish J. et al., A Digital Correlator Upgrade for the Arcminute

MicroKelvin Imager, 2018

Högbom J., Aperture Synthesis with a Non-Regular Distribution of Interferometric

Baselines., Astron. Astrophys. Supp. 15, 1974, p. 417-426

Ingalls J. et al., Using Drift Scans to Improve Astrometry, Proc. of SPIE Vol. 9143, 2014

Jackson N. et al., Royal Astronomical Society. Monthly Notices., 454, 2015, p. 287-298

Jackson N., Principles of Interferometry, University of Manchester,

Jodrell Bank Observatory, 2019

Jaynes E., Information Theory and Statistical Mechanics, Physics Review, vol. 106,

1957, p. 620–630

Kasuga T., Ishiguro M. & Kawabe R., Interferometric Measurement of Tropospheric

Phase Fluctuations at 22 GHz on Antenna Spacings of 27 to 540 m, IEEE

Trans. Antennas Propag., AP-34, 1986, p. 797–803

Madore B. et al., A Knowledgebase for Extragalactic Astronomy and

Cosmology, Caltech and Carnegie,

https://ned.ipac.caltech.edu/level5/-March14/Reid/Reid4.html,

accessed April 2021

Memon N., Neuhoff D. & Shende S., "An Analysis of Some Common Scanning

Techniques for Lossless Image Coding," in IEEE Transactions on Image Processing, vol.

9, no. 11, 2000, p. 1837-1848

Narayan R. & Nityananda R., Maximum Entropy Image Restoration in Astronomy,

Annual review of Astronomy and Astrophysics, vol. 24, 1986, p. 127–170

Pearson T. & Readhead A., Image Formation by Self-Calibration in

Radio Astronomy, IN: Annual Review of Astronomy and Astrophysics,

Volume 22. Palo Alto, CA, Annual

Reviews, Inc., 1984, p. 97-130

Perley R. et al., Astronomical Society of the Pacific, 1989, p. 178-179

Reid R., Smear Fitting: a New Image-Deconvolution Method for Interferometric Data,”

Monthly Notices of the Royal Astronomical Society, vol. 367, no. 4, 2006, p. 1766–

1780

Rottgering H. et al., “VLA Observations of the Rich X-Ray Cluster Abell 2256,”

Astrophysical Journal, vol. 436, 1994, p. 654–668

Rudelson M. & Vershynim R., Sparse Reconstruction by Convex

Relaxation: Fourier and Gaussian Measurements, 2006

Schwab F. & Roberts J., Indirect Imaging, Cambridge University Press,

1984, p. 333346

Schwarz F., Mathematical-Statistical Description of the Iterative Beam Removing

Technique (Method CLEAN), Astron. Astrophys. 65, 1978, p. 345-356

Scott P. & Ryle M., The Number-Flux Density Relation for Radio Sources Away from the Galactic Plane, Mon. Not. R. Astron. Soc. 122, 1961, p. 389-397

Tan S., An Analysis of the Properties of CLEAN and Smoothness Stabilized CLEAN--

Some Warnings, Mon. Not. Royal Astron. Soc. 220, 1986, p. 971-1001

Taylor G., Carilli C. & Perley R., Synthesis Imaging in Radio Astronomy, Astronomical Society of the Pacific, 1999

Thompson A., Moran J. & Swenson G., Interferometry and Synthesis in Radio

Astronomy, New York, John Wiley and Sons, 1986, p. 348

Waldram E. et al., 9C: A Survey of Radio Sources at 15 GHz with the Ryle Telescope, Monthly Notices of the Royal Astronomical Society, Volume 342, Issue 3, 2003, p.

915–925

Yen J. & Haykin S., Array Signal Processing, Prentice-Hall, Englewood Cliffs, NJ, 1985, p. 293-350

Zwart J. et al., “The Arcminute Microkelvin Imager”, Monthly Notices of the Royal Astronomical Society, Volume 391, Issue 4, 2008, p. 1545–1558

Glossary

This glossary is specific to running CASA tasks for AMI data reduction

action	Choice of PB-correction with spectral-index recalculation or only spectral-index recalculation (using the specified threshold)
actnoise	measurement of noise on the map, will be used to produce the noisemap
ami_array	which AMI array. Variations on SA and LA are accepted. Default for these observations is SA
archive	Name of the flux archive file

caltable	Name of the output calibration table
catfile	File to read source information from, currently in add_spec format: column 1 = source id, 2 = RA (sexagesimal with :), 3 = Dec (sexagesimal with :), 7 = Flux (mJy), 19 = spectral index (Cambridge), 20 = reference frequency (GHz)
chanlist	List of channel ids, within the above SPW ids, at which to make PBs
continuum	Create a single-frequency correction table (True) or add frequency dependence (False). Frequency dependent calibration tables must have the same number of channels as the ms and can be quite large.
cordir outdir	final raster maps
data_dir	the location where you're going to put your reduced datafiles and maps. This should have some subdirectories as described below.
do_plots	Whether to make plots as a visual check, default = False
drift	Is this a drift scan observation?
field	Field selection for the Primary Beam
fitsidi_dir	The location where the full-resolution, raw FITSIDI files of the drift
fitsidifile	Name of the input FITSIDI file containing rain gauge table
fitsin	data_dir+ami_array+'/drift/uvfits/' reduced quick-look uv-data
fitsin2	data_dir+ami_array+'/drift/fitsidi/' reduced full-resolution uv-data
gains_dir	/ami/'+ami_array+'/gains/' calibration files for reducing quick-look data
gains_dir2	data_dir+ami_array+'/bpass/' calibration files for reducing full-res data
git_path	'/scratch/YOUR_USERNAME/AMI/' the location you have the AMI git scripts in
workdirectory	frequencies, and Taylor-coefficient images that describe the PB spectrum.
incr	Whether to increment (True) or replace (False) existing model
inputfile=infile	Input FITS file to fit source parameters to. This is the reduced data from the drift scan, averaged down in frequency to 8 channels and exported in uv-fits format

inverse	Whether to correct for primary beam attenuation (False) or apply primary beam correction (True). Default is False.
nbins	Number of frequency bins to write in the flux archive file
noisemap	Input FITS noisemap to get pointing noises from. If not specified, the weights in the input uv-FITS file will be used to estimate noises.
nominal	Nominal rain gauge values, one per antenna. If not specified, read from default file for the appropriate AMI array, or the FITSIDI file header if not available
nterms	Number of Taylor terms to be used to model the frequency-dependence of the primary beam.
outdir	Pointing maps produced from quick-look data
outfile	Name of output primary beam corrected image.
outputvis	Name of the output visibility set, default: same as vis
pbcor	If True, primary beam correct the flux densities in the catalogue file
pblim	PB level below which to blank the image. Default 0.1
pbmin	PB gain level below which to not compute Taylor-coefficients or apply PB-corrections.
pointing	Name or number of pointing as referenced in ms
rainfile	Supply a .npy format file containing the rain gauge readings. Default is None, in which case read from the FITSIDI file
reffreq	Reference frequency about which the Taylor-expansion is defined.
reverse	Reverse the correction, i.e. undo a previously applied rai
rootname	Root for output filenames in chains directory. If not given, the stem of the input filename will be used
scalar	Perform scalar average over baselines instead of vector average (if calibration is poor and signal-to-noise is good). Default False.
showgui	Show the plot interactively if true, otherwise save to file
snr=snr_cut	Enter the minimum SNR sources must have to be fit. I think it is 5 by default
spwlist	List of SPW ids for which to make separate Primary Beams

swarp	The location where of the SWarp binary
threshold	Flux level in the restored intensity map, below which to not recalculate spectral index.
tsys	System temperature values to use in calculating the rain gauge correction. Shape of array should be (nant,nbin) where nbin can be any number. If not specified, read from default file for the appropriate AMI array, or the FITSIDI file header if not available
uvbin	Grid visibilities in uv-space before fitting
vis	Name of the input visibility set
weightlist	List of relative weights to apply to the PBs selected via the spwlist,chanlist parameters. Weights should approximately represent the sum-of-weights applicable during imaging each of these frequencies.
which_beam	Which beam parameterisation to use, Gaussian ('g') or AIPS ('a'). Default 'g'
write_archive	Option to write to an old-style flux archive file
wtsfile	Name of the .npy format file produced by read_wts_drift, containing sample information